



Transportation Research Division



Technical Report 14-02

Bridge-in-a-Backpack™

*Task 1: Investigation of Span Lengths up to
70 Feet*

Final Report – Task 1, August 2011

Technical Report Documentation Page

1. Report No. ME 14-02	2.	3. Recipient's Accession No.	
4. Title and Subtitle Bridge-in-a-Backpack™ Task 1: Investigation of Span Lengths up to 70 Feet		5. Report Date August 2011	
		6.	
7. Author(s) Keenan Goslin, P.E. Harold Walton Bill Davids, Ph.D., P.E. Roberto Lopez-Anido, Ph.D., P.E.		8. Performing Organization Report No. AEWC Report Number 12-04.749	
9. Performing Organization Name and Address University of Maine – Advanced Structures and Composites Center		10. Project/Task/Work Unit No. Project 17681.00 Task 1	
		11. Contract © or Grant (G) No. Contract # 2010*3692	
12. Sponsoring Organization Name and Address Maine Department of Transportation		13. Type of Report and Period Covered	
		14. Sponsoring Agency Code	
15. Supplementary Notes			
16. Abstract (Limit 200 words) The Bridge-in-a-Backpack™ has previously been demonstrated with short spans. The first constructed one, Neal Bridge in Pittsfield, Maine had a span of 34 feet. This task includes research and development that demonstrates the technology can be used safely with spans up to 70 feet. This required investigations into capacity of the bridge during construction, improvements to the manufacturing process such that larger diameter tubes can be produced, and verification of structural models for larger diameter tubes.			
17. Document Analysis/Descriptors Arch bridges, concrete filled FRP tubes, Bridge-in-a-Backpack		18. Availability Statement	
19. Security Class (this report)	20. Security Class (this page)	21. No. of Pages 62	22. Price

Bridge-in-a-Backpack™
Task 1: Investigation of Span Lengths up to 70 Feet
AEWC Project 749
PIN 017681.00

Prepared for:
Dale Peabody

Maine Department of Transportation
Office of Safety, Training, and Research
16 State House Station
Augusta, ME 04333
(207) 624-3305

AEWC Report Number
12-04.749

Aug 31st, 2011

Prepared by:

Keenan Goslin, P.E.
Harold Walton
Bill Davids, Ph.D., P.E.
Roberto Lopez-Anido, Ph.D., P.E.

An ISO 17025 accredited testing laboratory
Accredited by International Accreditation Service



Bridge-in-a-Backpack™

Task 1: Investigation of Span Lengths up to 70 Feet

The Bridge-in-a-Backpack™ has previously been demonstrated with short spans. The Neal Bridge in Pittsfield, Maine had a span of 34 feet. This task includes research and development that demonstrates the technology can be used safely with spans up to 70 feet. This required investigations into capacity of the bridge during construction, improvements to the manufacturing process such that larger diameter tubes can be produced, and verification of structural models for larger diameter tubes.

Task 1.1 Modeling and Testing of the Filling Process

One objective of this Task is to assess the structural response of the thin-walled FRP shells used for buried arch bridge structures during concrete filling. The concrete is a liquid when it is first pumped into the arch. It conforms to the shape of its container, as dictated by gravity, and does not help carry bending, axial or shear stresses. Compressive stresses in the concrete will also be expelled as pressure into the walls of the FRP. These forces make the FRP susceptible to failure, not as a concrete filled member, but as a hollow section.

Two distinct fill methods have been used for arches: filling through a drilled hole in the crown or through a PVC pipe cast into the footing of the arch. Filling from the crown results in loading that is close to symmetric on each side of the arch reducing the likelihood of side-sway buckling, but requires a hole at the crown for concrete entry. In the past this hole has been roughly 3 inches in diameter. To avoid cutting the FRP for filling, concrete can also be pumped through a PVC pipe cast through the footing and into the base of the arch. The height of the PVC pipe exceeds that of the arch apex, and hydrostatic pressure drives the filling. Loading from a single side creates asymmetric forces that increase the risk of global buckling failure such as side-sway or snap through of the arch. Focusing on expected stress and capacity, there is no clear answer as to which filling method will create the safest arch filling, because crown filling puts a hole at a critical stress location and filling from the footing creates higher stresses from the asymmetric loading.

A computer model was constructed to predict the load and the resulting stress throughout the arch filling process. The model relies on beam elements, and tracks the loads on the arch during filling while treating the concrete as an ideal fluid whose top surface remains level. An enhanced method of predicting cross-sectional ovalization is also derived that considers both bending-induced curvature and initial curvature of the arch. The results of this model are compared with full-scale arch fill tests conducted in the laboratory and the field for a nominally identical arch.

Defining the Model

The model used for determining the loads on the structure uses small deformation, two-noded beam elements. These elements do not incorporate shear deformations, only bending deformations. This model was compared against a three-noded beam element used as part of PressArchAnalysis developed at the University of Maine (Davids, 2009) that includes shear deformations and large displacements. Due to large span to depth ratio (~30:1), it is projected that bending deformations will dominate the response. Deflections measured in the lab are small; it is not expected that a small deformation analysis will give a significant loss in model accuracy. All computer code for this model is based in MATLAB (Walton 2011).

The main function in the code has the option of running either the two-noded element or writing an input file to PressArchAnalysis to use the three-noded element. The advantages of the two-noded elements are faster run time, faster element convergence, and the ability to move or rotate supports if desired. The disadvantage is the inability to account for shear deformation in the analysis. However, shear deformations of the arch shell are quite small, so this is not a significant limitation.

Nodal Position

Present bridge arches are partial circular arcs defined by a radius and a turned angle; these two quantities define the span and the depth of the arch, as depicted in Figure 1. For the Belfast Bridge, the case study for this model, the radius R was 31.27ft and the angle β was 99.2 degrees. Nodes were spaced evenly along the length of the arch (first node in the left footing, last node in the right footing) based on the number of elements desired in a given analysis with an assigned horizontal and vertical measurement from the left footing.

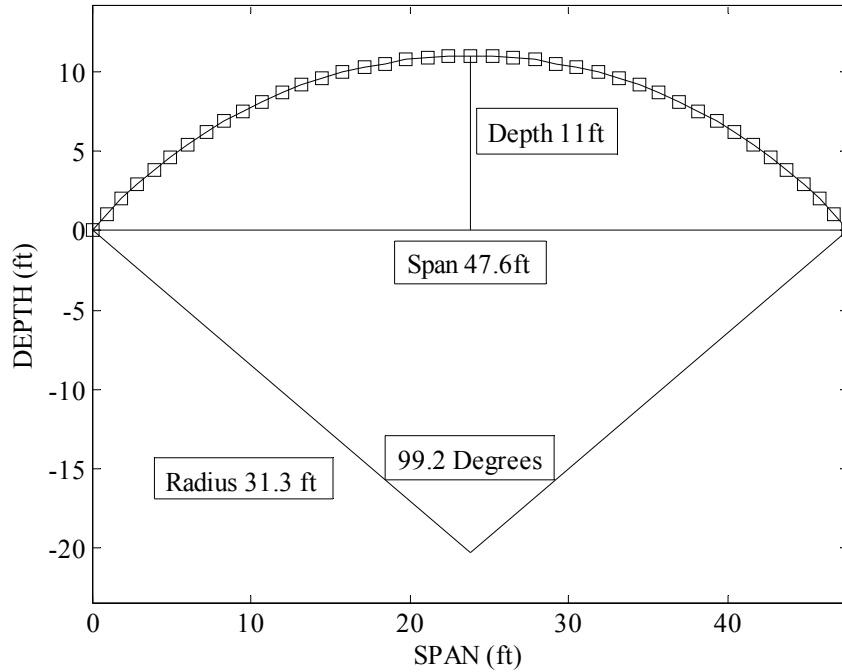


Figure 1. Arch Geometry

Laminate Properties

No experimental data exists for the elastic properties ($E_x, E_\theta, \nu_{x\theta}$) of the laminate used in the Belfast Bridge arches. Classical Lamination Theory was used to calculate the elastic properties of the laminate (Walton 2011). MATLAB code was written to calculate critical material properties from assumed input parameters, and the program output is in Table 1.

Table 1. Properties of Belfast Carbon and E-Glass

Property	Carbon	E-Glass	Laminate
Angle (Degrees)	16	76	-
Thickness (in)	0.038	0.039	0.115
E_x (ksi)	12700	1600	9200
E_θ (ksi)	1800	5000	2900
$\nu_{x\theta}$	0.767	0.138	0.366
$G_{x\theta}$ (ksi)	1500	800	1200

Load Distribution

The fluid weight of concrete contributed most to the load on the unfilled arches. The concrete was treated as a frictionless fluid that instantly self levels making the surface of

concrete perpendicular to gravity. Load was assessed on a per-node basis from the volume of concrete and using 144 lb/ft³ for concrete density. The volume of concrete was stepped linearly during the fill with the number of load steps equaling number of nodes, although these values need not be related. Total concrete volume was divided into left and right side concrete volumes; at this time three different conditions (sequential fill, even fill, even fill +2.03ft arc length) were selected for concrete side distribution. For each side of the arch volume distribution over the nodes is determined by elevation. The volume at each node in a half arch was calculated for a given fill elevation and a Newton iteration was used to recalculate the elevation until the total distributed volume equaled the desired volume for that side.

Nodal volumes were assessed on a tributary length basis using half the distance between the nodes on each side of the node of interest, Figure 2. For a completely filled section, concrete elevation above the highest cross section elevation for a given node, the unit volume V_u was calculated using cross sectional area (circle) times tributary length L_i . Tributary length in Equation 1 is calculated using the turning radius R , the number of nodes n and the total angle of rotation for the arch β .

$$L_i = \frac{2\pi}{n\beta} R \tag{Equation 1}$$

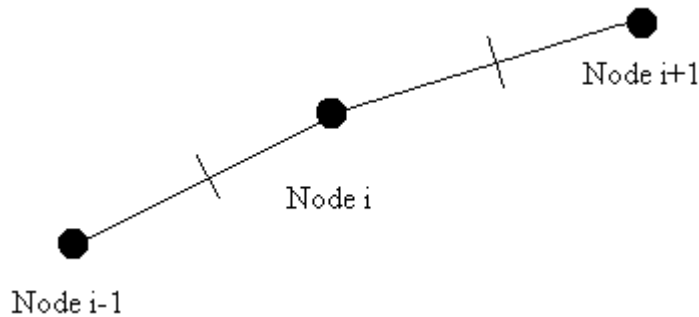


Figure 2. Tributary Length to Node i

For a partially filled section a more complicated process was implemented. Volume was calculated by summing (using an integral) the partial circular areas A_p over a tributary length. All calculations are based on a single independent variable ϕ , the clockwise angle measure from the left horizontal global radius. The left horizontal radius is the base of a 180-degree arch; it lies below the base of a smaller angle arch. Over the partially filled section, elevation of concrete remained constant. Fill depth d_p depends on global radius R , local radius r and angle ϕ , the only independent variable, as in Equation 2.

$$d_p = \frac{R}{\sin(\varphi)} - R + r \tag{Equation 2}$$

For a given depth of filled concrete there is a unique area defined by a circular segment as shown in Figure 3. An intermediate variable, angle of filled section α (shown in Figure 3) is calculated in Equation 3 using the depth of filled concrete and local radius. Partial area, Equation 4, is based on filled angle and cross section radius.

$$\alpha = 2 \arcsin\left(\frac{d_p}{r} - 1\right) + \pi \tag{Equation 3}$$

$$A_p = \frac{r^2}{2}(\alpha - \sin(\alpha)) \tag{Equation 4}$$

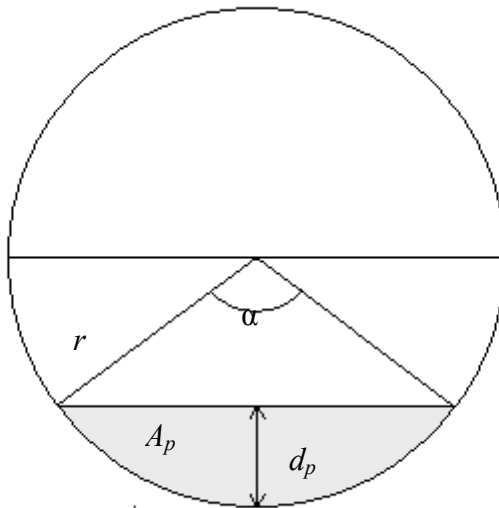


Figure 3. Partially Filled Cross Section

The total volume of the partially filled section is based on an integral in terms of turned angle from global horizontal radius to point of interest, φ , where φ is the only independent variable. The upper and lower limits of the integral, φ_f and φ_e , are the angles were the tube becomes fully filled and fully empty respectively. This definite integral was solved using Gauss quadrature.

$$V_p = \frac{R}{2\pi} \int_{\varphi_f}^{\varphi_e} A_p d(\varphi) \tag{Equation 5}$$

Many times, the partially filled section spanned multiple nodes. Instead of using the absolute minimum and maximum angles, the limits changed based on whether the upper rear corner and lower front corner of the tributary area were ‘wet’ or ‘dry’. As many nodes were used, all loads over a partial area were pooled at the node. Figure 4 shows the four possible partially filled sections. When the upper rear corner is wet (b, c) the lower limit was the absolute minimum angle φ_f and a portion of a completely filled section was added to the integral representing the filled area in the lower side of the section. When the upper rear corner is dry (a, d) the lower limit was the minimum angle for the node φ_{min} . When the lower front corner was wet (c, d) the upper limit was the maximum angle for the node φ_{max} , while the maximum fully empty angle, φ_e , was used when the lower front angle was dry. The following equations show the integral modified for case (a) Equation 6, (b) Equation 7, (c) Equation 8, and (d) Equation 9.

$$V_{(a)} = \frac{R}{2\pi} \int_{\varphi_{min}}^{\varphi_e} A_p d(\varphi) \tag{Equation 6}$$

$$V_{(b)} = V_u \left(\frac{\varphi_f - \varphi_{min}}{\varphi_{max} - \varphi_{min}} \right) + \frac{R}{2\pi} \int_{\varphi_f}^{\varphi_e} A_p d(\varphi) \tag{Equation 7}$$

$$V_{(c)} = V_u \left(\frac{\varphi_f - \varphi_{min}}{\varphi_{max} - \varphi_{min}} \right) + \frac{R}{2\pi} \int_{\varphi_f}^{\varphi_{max}} A_p d(\varphi) \tag{Equation 8}$$

$$V_{(d)} = \frac{R}{2\pi} \int_{\varphi_{min}}^{\varphi_{max}} A_p d(\varphi) \tag{Equation 9}$$

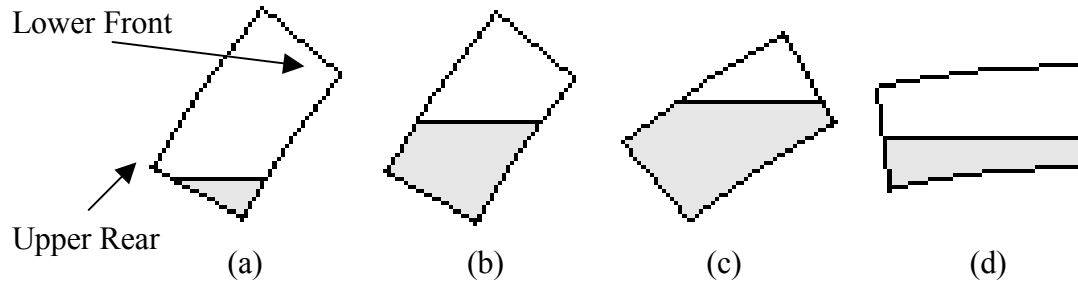


Figure 4. Different Partially Filled Sections

A limitation of this analysis was that, even with the thin concrete mix used for arch filling, concrete pools at the apex where the arch is perpendicular to gravity, and this model neglects this load. The program allows for surcharge loads, but none were applied in this analysis.

In the field, the surcharge may be higher due to a thicker concrete mix and/or additional load from people and equipment on the arch. Three to four men were near the apex of the arch during filling, and while their load was spread to adjoining members, the instrumented arch shows load effects at and before the start of filling.

Additional dead loads were not considered in this analysis because dead loads are applied before instrumentation, but they should be considered for predicting maximum stress. To predict lab filling a distributed load of 0.47lb/ft, based on the weight of the composite arch, was added for self-weight and in the field a load of 2.33lb/ft, based on self weight and decking weight.

Stress and Strain

A practical output for this analysis is either the stress envelope for design or the strain envelope for comparison to experimental results. Failure load can be converted easily to failure stress, and stress is a common way to represent failure. Strain is better for comparison to experimental data because strain can be directly measured, unlike stress, and so elastic modulus only needs to be assumed in the model, not in the experimental results. Stress is calculated from the axial force and moment at each node. Where σ is stress, P is axial force, and M is internal moment. Equation 10 gives total stress.

$$\sigma = \frac{Mr}{\pi(r^4 - (r-t)^4)} + \frac{P}{2\pi rt} \tag{Equation 10}$$

Strain ‘ ϵ ’ is related to stress by the elastic modulus, Equation 11.

$$\varepsilon = \frac{\sigma}{E_x}$$

Equation 11

Ovalization

Initial preliminary investigations into ovalization showed that there could be a loss in moment capacity of the section by up to 15%. Ovalization is the shape change of the round cross section with increases in bending forces on the section. Brazier (1927) investigated hollow beam sections and showed the ovalization had a shortening effect on the cross section thus reducing the bending capacity of the member. Because of time constraints two tasks were conducted to control and assess ovalization. For the control of ovalization during arch filling, clamps were designed for restricting shape change of the hollow FRP tubular arch used in testing as described later in Task 1.3. As part of a longer-term effort, an analytical and experimental approach to quantifying ovalization was developed and is discussed in the present section. This rigorous analytical and experimental approach shows that for the tubes presently in use ovalization is negligible during construction loading.

Prior testing of fluid filled straight tubes showed negligible radial ovalizations up to failure. However, ovalization occurs as bending stress acts through the curved beam, and with an arch the effect is magnified due to the initial curved shape. Brazier (1927) assumed that curvature was directly related to bending moment, as it is for a beam, and that the material was uniform (isotropic), both properties that do not apply to the arches. An arch has an initial curvature much higher than the bending curvature in a typical beam and the material is anisotropic. No reference has been found on ovalization for tubes curved when in the at rest position, so a modified ovalization prediction was developed for this case using the same approach originally used by Brazier (1927). In this approach, potential energy U is minimized with many small terms and symmetric terms ignored. The arch composite is treated as orthotropic, and the cross-section is assumed to be loaded in pure bending. In the following formulation, all terms ignored are the same as the terms ignored by Brazier. Brazier wrote all equations in terms of two variables, angular cross section shift s , and angle of rotation from vertical θ . Formulas use w as local radius change, κ as curvature, κ_{bend} as bending curvature – related to moment, κ_{θ} as radial curvature – curvature of the cross section, D_{22} as transverse bending stiffness, ν as Poisson's ratio, ψ as distance from the center of the cross section to the shell edge, and E_{θ} as radial elastic modulus. Bending curvature and total curvature, calculated in Equation 12 and Equation 13, are used later for forming the potential energy equation.

$$\kappa_{\text{bend}} = \frac{M}{E_x I_x} \quad \text{Equation 12}$$

$$\kappa = \kappa_{\text{bend}} + \frac{1}{R} \quad \text{Equation 13}$$

Initial cross section displacements are caused by deformation of the cross section under bending stress from Poisson's ratio. These displacements are small, (order $r/1000$) compared to ovalization, but they are the foundation for calculating transverse curvature. Initial radial deflection is Equation 14 and initial deformation in the angular direction is Equation 15.

$$w_0 = \frac{\kappa_{\text{bend}}}{2} \nu r^2 \cos(\theta) \quad \text{Equation 14}$$

$$s_0 = -\frac{\kappa_{\text{bend}}}{2} \nu r^2 \sin(\theta) \quad \text{Equation 15}$$

Angular change and radial change are related by a derivative if the cross section does not stretch during filling, Equation 16. This allows the full equation for radius change to be written as Equation 17.

$$w' = \frac{ds'}{d\theta} \quad \text{Equation 16}$$

$$w = \frac{ds}{d\theta} + \frac{\kappa_{\text{bend}}}{2} \nu r^2 \cos(\theta) \quad \text{Equation 17}$$

Radial displacement is differentiated twice to get radial curvature Equation 18. Radial curvature is rewritten in terms of differential variables, Equation 19.

$$\frac{d^2 w}{d\theta^2} = \frac{d^3 s}{d\theta^3} - \frac{\kappa_{\text{bend}}}{2} v r^2 \cos(\theta) \quad \text{Equation 18}$$

$$\kappa_{\theta} = \frac{1}{r^2} \left(\frac{d^2 w'}{d\theta^2} + \frac{ds'}{d\theta} \right) \quad \text{Equation 19}$$

Substitute values from previous equations to get Equation 20.

$$\kappa_{\theta} = \frac{1}{r^2} \left(\frac{d^3 s}{d\theta^3} + \frac{ds}{d\theta} \right) \quad \text{Equation 20}$$

Cross section bending stiffness D_{22} , Equation 21, is needed, with κ_{θ} , to calculate energy of cross section deformation.

$$D_{22} = \frac{E_{\theta} t^3}{12(1 - \nu_{12}\nu_{21})} \quad \text{Equation 21}$$

Since this analysis treats the cross-section as if it is under pure bending, load potential arose only from the longitudinal bending moment in the arch. This value depends on moment acting through local rotation change. A necessary value is the distance to the center of the cross section from any point on the edge $\psi(\theta)$, Equation 22.

$$\psi(\theta) = (r - w)\cos(\theta) - v\sin(\theta) \quad \text{Equation 22}$$

Both change in rotation $\gamma(\theta)$ Equation 23 and longitudinal (arc length direction) internal moment, as a function of cross section rotation, $M_x(\theta)$ Equation 24, depend on d .

$$\gamma(\theta) = \frac{\kappa\psi(\theta)}{\pi r} \quad \text{Equation 23}$$

$$M_x(\theta) = E_x \kappa_{\text{bend}} \pi t r^2 \psi(\theta) \quad \text{Equation 24}$$

The lateral curvature κ_{θ} and the longitudinal internal moment $M_x(\theta)$ are combined in a potential energy equation.

$$U = \int_0^{2\pi} \left(rD_{22} (\kappa_\theta(\theta))^2 + M_x(\theta)\gamma(\theta) \right) d\theta \quad \text{Equation 25}$$

Values are substituted into Equation 25, resulting in Equation 26 and Equation 27. Equation 27 was simplified by removing any ‘small’ terms, meaning all terms with Poisson’s effect raised to a power.

$$U = \int_0^{2\pi} \left(\frac{E_\theta t^3}{12(1-\nu_{12}\nu_{21})r^3} \left(\frac{d^3s}{d\theta^3} + \frac{ds}{d\theta} \right)^2 + \kappa\kappa_{\text{bend}} r^2 t E_x \psi(\theta)^2 \right) d\theta \quad \text{Equation 26}$$

$$\psi(\theta)^2 = \left\{ r - 2 \left(\frac{ds}{d\theta} + r\nu \cos(\theta) \right) \right\} \cos^2(\theta) - s \sin(2\theta) \quad \text{Equation 27}$$

To minimize potential energy, ‘s’ must satisfy Equation 28 found using calculus of variations.

$$\frac{d^6s}{d\theta^6} + 2 \frac{d^4s}{d\theta^4} + \frac{d^2s}{d\theta^2} = - \frac{18r^5 \kappa\kappa_{\text{bend}} E_x}{t^2 E_\theta} (1 - \nu_{12}\nu_{21}) \sin(2\theta) \quad \text{Equation 28}$$

The solution to this follows the form in Equation 29.

$$\frac{d^2s}{d\theta^2} = (A + B\theta)\cos(\theta) + (C + D\theta)\sin(\theta) - \frac{N}{9} \sin(2\theta) \quad \text{Equation 29}$$

It follows that N is satisfied by the right hand side of Equation 28.

$$N = \frac{18r^5 \kappa\kappa_{\text{bend}} E_x}{t^2 E_\theta} (1 - \nu_{12}\nu_{21}) \quad \text{Equation 30}$$

Values B, C, D, and the first constant of integration cancel out due to symmetry and continuity of the cross section. A, and the second constant of integration, are rigid body displacements that do not contribute to ovalization. The integration for s is completed in Equation 31.

$$s = \frac{r^5 \kappa \kappa_{\text{bend}} E_x}{2t^2 E_\theta} (1 - \nu_{12} \nu_{21}) \sin(2\theta) \quad \text{Equation 31}$$

The radius change, w is related to s by Equation 17. The second term is discarded, as it is much smaller than the first term for an arch. Radius loss is in Equation 32, vertical radius loss corresponds to $\theta = 0$.

$$w = \frac{r^5 \kappa \kappa_{\text{bend}} E_x}{t^2 E_\theta} (1 - \nu_{12} \nu_{21}) \cos(2\theta) \quad \text{Equation 32}$$

This resulting ovalization equation was implemented for comparison to experimentally measured ovalization. Future work is needed to include the effect of the deformed cross section on the concrete volume distribution or to use the moment of inertia of the deformed section in the beam stiffness model. An implication of this reworking of Brazier's equations is that ovalization can both reduce the vertical radius and increase the vertical radius because, unlike a beam, bending curvature and total curvature are not equal for an arch. Total curvature is much larger than bending curvature and does not depend on the sign of the moment; for geometries explored here, the arch would buckle well before the curvature stopped being concave down at any point. When moment is positive (compression on top) the vertical radius will expand, increasing section modulus and reducing bending stress. When the moment is negative, the cross sectional height will decrease, increasing bending stress. During filling, the sign of the moment shifts at least once in all points of the arch, and during filling there will be transition regions from positive to negative bending in the arch and therefore sections that become deeper and sections that become shallower.

Beam Model Validity versus Other Models

A model was constructed in RISA 2D to compare with the two-noded, two-dimensional beam element model. The goal was to verify that for a given load the deflection, moment, and axial load calculated by the beam element model was acceptably close to a common structural analysis tool. The material and geometry properties of the arch matched the Belfast Bridge. Both models had 41 nodes and the same node locations corresponding to a centerline span of 47.6ft and a turned angle of 99.1 degrees. All models had fixed end conditions on both footings of the arch and utilized the same material and geometric constants: I (143 in⁴), A (5.35in²), and E_x (9.21ksi). Two loading options were considered, one with a 1000 lb point load at the apex, the other with an even load applied to each node corresponding to a completely filled arch (225 lb). Axial load, moment, and deflection were compared at the footing and the apex of the arch for both models in Table 2.

Table 2. Comparison between RISA Model and Beam Models

Model Comparisons		RISA-2D	2-Noded	% Difference
Concrete	Axial foot (kip)	6.32	6.32	0.0633
	Axial crown (kip)	4.56	4.56	0.0853
	Moment foot (kip-ft)	1.14	1.14	0.219
Fully Filled	Moment crown (kip-ft)	0.93	0.94	0.317
	Deflection crown (in)	0.11	0.11	0.901
1000 lb	Axial foot (kip)	1.03	1.03	0.0774
	Axial crown (kip)	1.00	1.00	0.0797
	Moment foot (kip-ft)	1.63	1.63	0.0286
Point load	Moment crown (kip-ft)	2.61	2.61	0.0246
	Deflection crown (in)	0.09	0.09	0.232

Results from the two models are very similar suggesting that the MATLAB models is generating the proper load effects. The highest difference seen between the two-noded and RISA models was 0.9%, apex displacement for a fully filled arch. Much of the difference may come from round off error; RISA only reports two figures for this value, to two figures both analyses produce the same value.

The value of using MATLAB models instead of RISA models is apparent when modifying model assumptions and implementing additional analyses, such as ovalization, that would require a more complicated analysis than RISA can easily incorporate, and indeed might require a full 3-dimensional model based on shell elements to capture with commercial software. The beam element models can also be easily modified to run several similar analyses and compare results automatically. They are primarily used to create stress envelopes over the course of filling the arch, requiring many separate RISA modifications, while only needing a driver file in MATLAB with the separate loads.

Different Loading Scenarios

There are two main filling scenarios: either the arch is filled through a hole drilled at the apex or it is filled from a single footing through an atmospheric pressure standpipe or pressurized valve. The first method has the disadvantage of drilling a hole in one of the critical moment locations of the arch, which considerably reduces the buckling capacity of the FRP shell. However, the maximum stress at the footing is generally lower when the arch is filled from the apex, reducing the maximum stress in the arch when compared to footing filling.

Three load cases were considered in models: fill case 1, the arch is filled from a single footing, fill case 2, the arch is filled symmetrically from the crown, fill case 3, the arch is filled from the crown but flow is not even and the left side fills faster (additional 2.03ft arc length filled) than the right side. The model always considers the left side to have more concrete in an uneven fill, but this is an arbitrary designation as the arch is symmetric. If, in practice, the arch were filled more rapidly from the right side, the model results could be inverted without any change in result.

The modeled offset is the same as the allowable unbalance in the design specifications for the arch filling procedure. After both sides of the arch are filled to the base of the apex (~70% full) the load for the remainder of the fill is identical. The following plots show the maximum moment and strain along the length of the arch for both filling methods as well as stress envelopes for the left footing, left shoulder (20% of total span) and mid span.

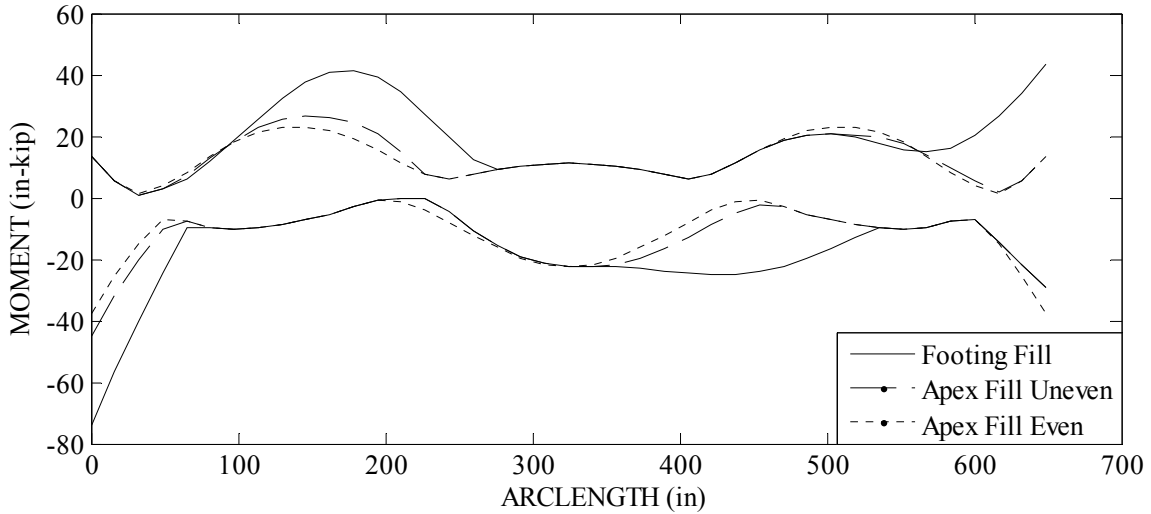


Figure 5. Maximum Moment from Filling Along Length

Fluctuation in stress over the length was primarily determined by moment. Axial stress increased throughout the fill as additional concrete was added, but it was rare for the axial footing stress to exceed the lowest axial stress by more than 50%.

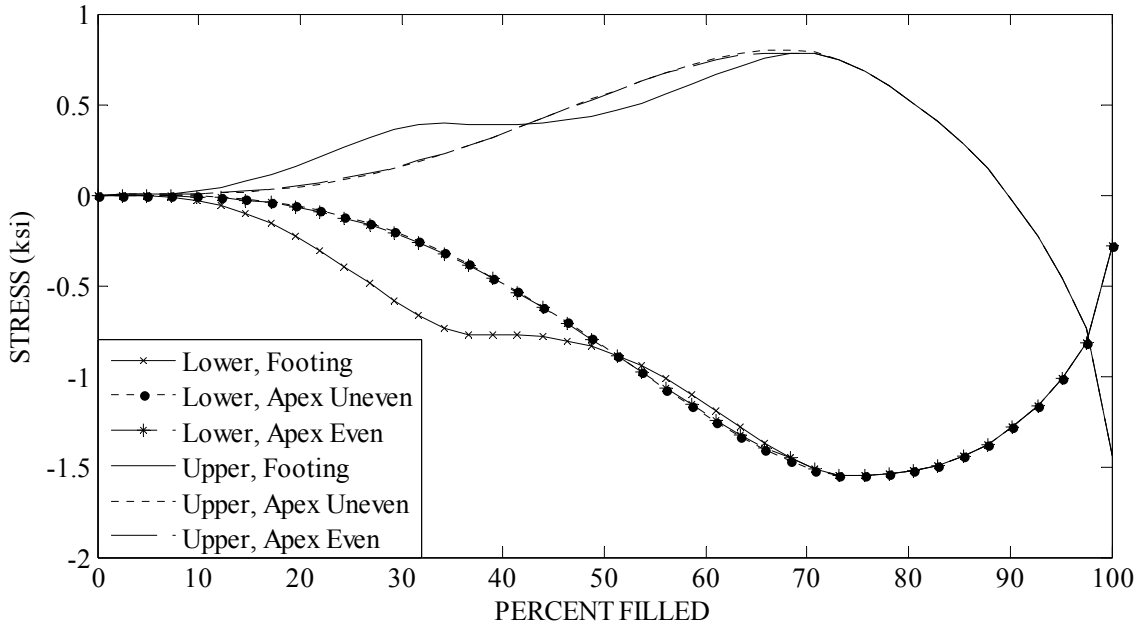


Figure 6. Apex Stress Envelope, Different Fill Methods

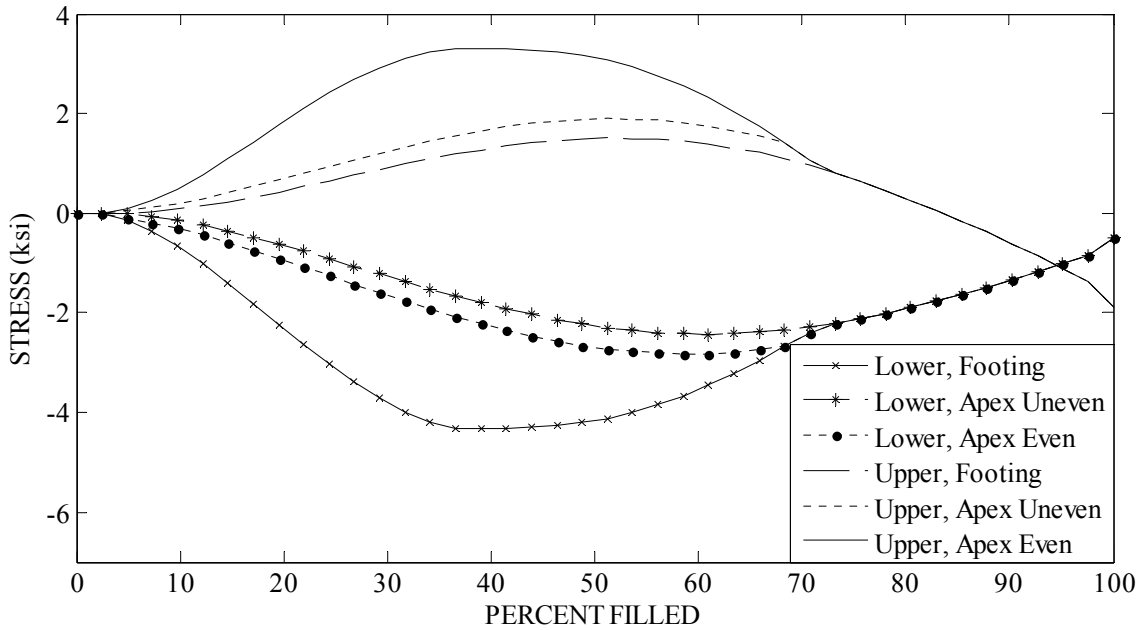


Figure 7. Footing Stress Envelope, Different Fill Methods

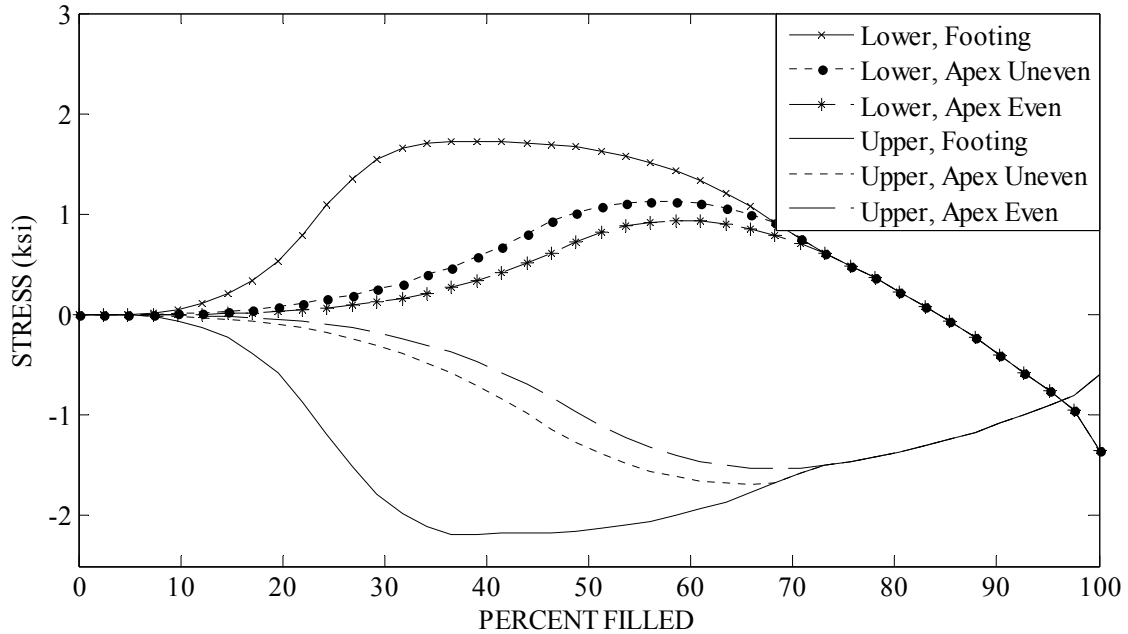


Figure 8. Shoulder Stress Envelope with Different Filling Methods

For the Belfast Bridge, one-sided filling puts the critical stress at the left footing, increasing the peak footing stress from 2.18 ksi in an even fill to 4.35 ksi. However, peak stress at the apex for either fill was 1.52 ksi, and with a hole drilled at the apex, this defect may be critical. Based on experimental testing results that show a 40% reduction in capacity with a scaled hole in a smaller tube, the apex stress should control for the apex fill by a small margin – the equivalent apex stress is 1.31 ksi for the 2.18 ksi footing stress. When considering a 40% reduction, the footing stress from the footing fill is equivalent to a 2.61 ksi stress in the reduced capacity section making the stress at the footing considerably higher than the worst-case load for the apex fill.

Filling Measurements Laboratory and Field

A bridge built in Belfast, Maine over the Little River was constructed with 16 carbon fiber/glass fiber arches with turning radius 31.27ft and turned angle 99.3 degrees. In preparation for the bridge, a single arch was filled in the lab to confirm filling capacity and load effects. All arches were fabricated with a braided e-glass diameter constraint layer (+/-75 degrees, 0.039in) and two braided carbon fiber structural layers (+/-16 degrees, 0.038in/layer). Figure 9 has a picture of the arch before filling in the lab and Figure 19 has a picture of the Belfast Bridge during filling.

Laboratory Fill

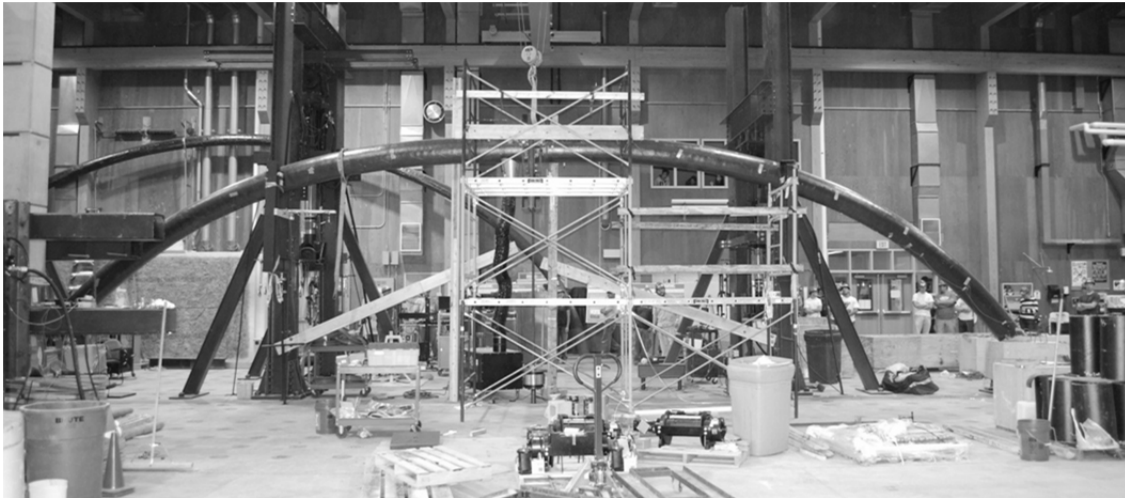


Figure 9. Arch Erected in Lab for Concrete Fill

Test Setup

Along with a fill test, the arch was also tested after the fill concrete cured with a point load at the crown to find maximum bending capacity. In this second strength test, the arch was loaded by an actuator mounted under the floor pulling down on the center of the arch. Pinned supports were bolted to the floor 50ft apart. Both supports were blocked with wooden restraints to resist rotations, during concrete placement in the footings. Once the arch was positioned, the arch footings were cast in a typical 4000psi concrete mix and allowed to cure for a week before filling the arch. In the graphs displayed here, support rotation was not considered.



Figure 10. Right Footing of Arch during Lab Fill

The arch was filled with expansive, normal weight concrete with a measured slump-flow of 30” and a density of 144lb/ft³. Concrete entered the arch through a 3.0in diameter hole drilled at the apex of the arch. An attempt was made at directing concrete flow to the left and right hand sides of the arch, alternating flow direction when concrete height reached pre-drilled weep holes 4.07ft along the centerline arc length of the arch, Figure 11. The total elapsed time for concrete to reach a weep hole and the change in time from the previous location is recorded in Table 3. The first time, left and right, are both longer than the typical fill time, indicating that much of the early concrete placed in the arch had collected at the apex. After this fill step, the remaining fill heights occurred over a range of 57s to 65s for both the left and right side, indicating that the flow rate was nearly constant. Results indicate that the flow could not be directed for the duration of the test. After the initial two elevation steps, the surplus concrete at the apex prevented directional flow and the additional concrete filled both sides nearly evenly. This is visible from the recorded fill times, if concrete were only going in the directed side the change in time for left and right sides would be close to equal. After the second arc length step, the left side takes much longer to fill, four or five times longer than the right side, showing that the right received at a minimum 37% of the concrete intended for the left side. This result was not entirely negative; while indicating difficulty in directing flow to a desired side, it also indicated that even when an effort was made to direct flow, the arch still wanted to fill evenly. Even filling has lower stresses than directional filling giving a lower risk of failure.

Table 3. Fill Times for Each Arch Side

Filled Arc Length (ft)	Total Time	Total Time	Change in Time	Change in Time
	Left (s)	Right (s)	Left (s)	Right (s)
4.07	77	119	77	42
8.14	149	176	30	27
12.20	228	240	52	12
16.27	295	305	55	10
20.34	358	369	53	11
Full	459	459		



Figure 11. Concrete Measuring Locations (Crosses)

Instrumentation

Several measurements were taken during arch filling. Three critical areas were determined in the arch: near the footing, apex, and shoulder. The footing was predicted to have the peak stress and the peak axial load, the apex was predicted to have a large moment and the peak deflection, and the shoulder was predicted to have the highest moment. In the Belfast arch, the shoulder was 13.45ft along the center arc length from the arch footing, about a quarter of the span.

To be able to calculate stress in the arch, 0.98in quarter bridge foil strain gauges were attached at the three critical locations. At each location a gauge measured longitudinal top fiber, bottom fiber, and cracked-concrete neutral axis strain (for an ultimate load test). At the footing an additional strain gauge measured radial strains. Strain gauges were only attached to the north side of the arch.

Displacements were measured with string pots. All string pots were connected to the mid height of the arch (neutral axis) to avoid measuring ovalization and reduce measurement error unless otherwise noted. At mid span two string pots measured vertical arch displacement and a third gauge out of plane motion. At each shoulder two string pots were connected to the mid height of the arch cross section in plane with the arch, a measured distance from the arch. These gauges measured the vertical and horizontal translation of the arch during filling; it was assumed that there was no out of plane translation. Two additional string pots were used to measure ovalization, change in cross sectional depth, at two critical stress locations, the left shoulder and the mid span. Both ovalization measurements used wooden yokes that were taped directly to the top of arch with the string pot mounted on the bottom of the yoke and tied to the bottom face of the arch.

Results

Results for laboratory testing are presented as graphs plotted alongside model predicted values. Model predictions use two-noded elements, using the loading assumptions of the previous chapter. No surcharge loads were added, including load from concrete pooling at the apex. All graphs contain the raw data from the August fill test, not averaged data, so in some circumstances the data can have high fluctuation over a short time period. Data from the laboratory fill test is presented as strains or displacements. Model strains are presented as a strain envelope plotted with the top fiber and bottom fiber strain. The top and bottom fiber strains should ideally match the envelope. The neutral axis gauge was installed closer to the top axis, so the neutral axis strain should be similar to the top strain. Strains were used instead of stresses or moments so that predicted stiffness would have minimal effect on the presented results and that the data from the filling test could be presented without modification. Figure 12 through Figure 14 are strain plots for the apex, shoulder, and footing.

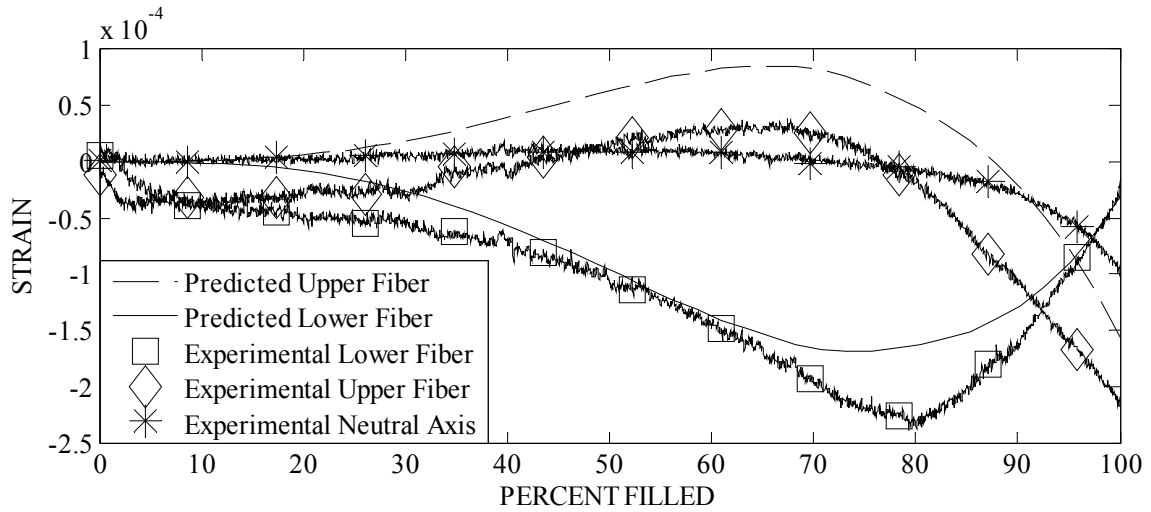


Figure 12. Apex Strain, Model and Laboratory

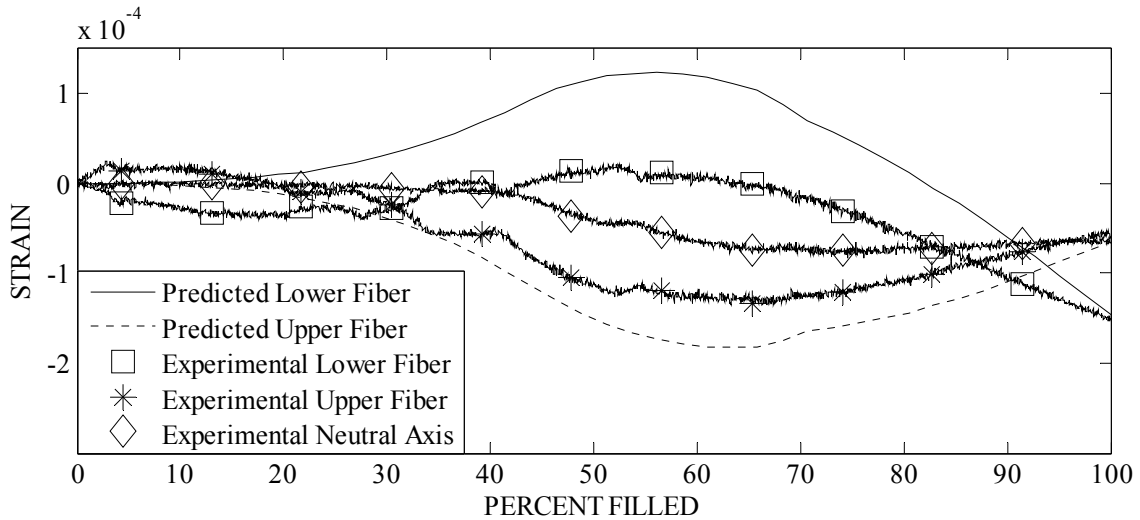


Figure 13. Shoulder Strain, Model and Laboratory

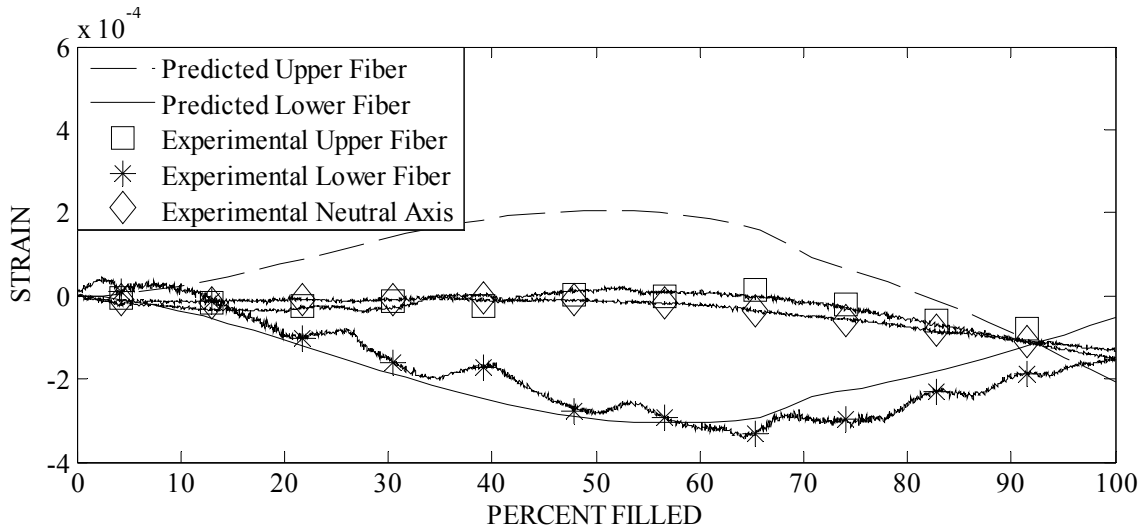


Figure 14. Footing Strain, Model and Laboratory

Strains did not exactly match the model predictions, but in some circumstances the model and the experiment exhibited good agreement. Strain at the apex was well predicted by the model. Both the top fiber gauge and the bottom fiber gauge follow the same shape as the model and give a good estimate of the final strain, although the top fiber gauge did not show as much tension throughout the test as predicted. Strain at the footing suffered from measurement difficulties. Gauges were attached around the circular cross section, but at the footing there is a high amount of variability in stress between the top axis and the bottom axis. The bottom gauge was installed ~ 2.76 in away from the footing, the top gauge was installed ~ 15.75 in away from the footing in order for both gauges to be installed on the same circular cross section. As a result of the distance from the footing, the lower fiber gauge is reading a stress similar to the model-predicted shell/footing interface stress, while the top gauge is reading a stress away from the peak moment of the footing. An inability to model the footing/shell interaction is a limitation of the beam element model. Predicted shoulder strains are higher than the measured shoulder strains, but still follow the same general shape. The strain varies rapidly with location at the footing, but more in terms of when the peak moment is achieved than the magnitude of the peak moment. Moment was much lower in the experimental arch than in the model prediction.

A possible explanation for some of the irregularity is out of plane strains. The arch had limited restraint from out of plane motion and it is possible that out of plain moments could develop as the arch started to sway. Little out of plane motion was observed while the arch was filling.

Displacement was measured at the apex and both shoulders. In general, predicted the displacement measurements are further removed from the predicted values than the strain. Strains were predicted better at the end of the test, when strains are critical – deflections were predicted more poorly at the end of the test than the beginning, possibly a sign of support movement. Deflections are presented as the model predicted

displacement and the actual instrument displacement. Figure 15 through Figure 17 show displacement: apex, left shoulder, right shoulder. Figure 18 is ovalization at both the apex and the shoulder of the arch.

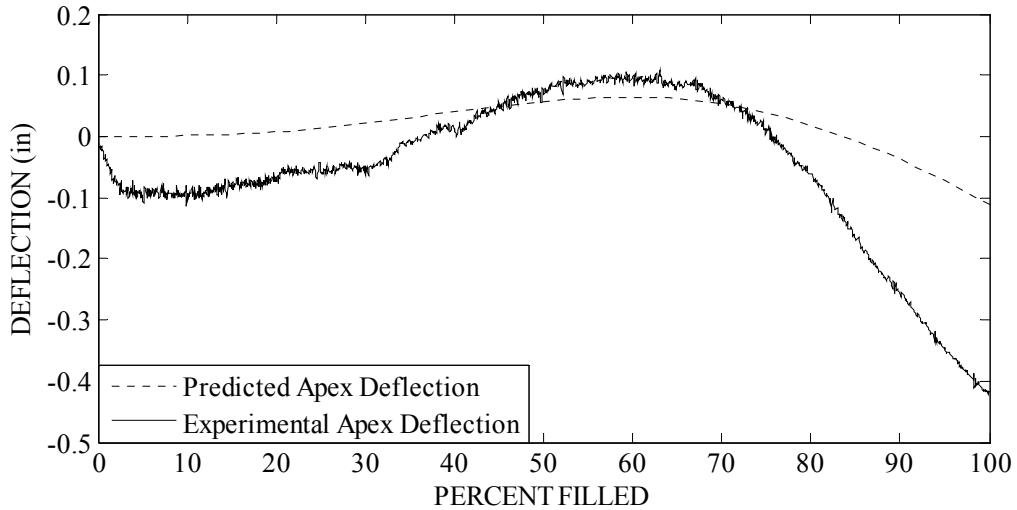


Figure 15. Crown Displacement, Model and Laboratory

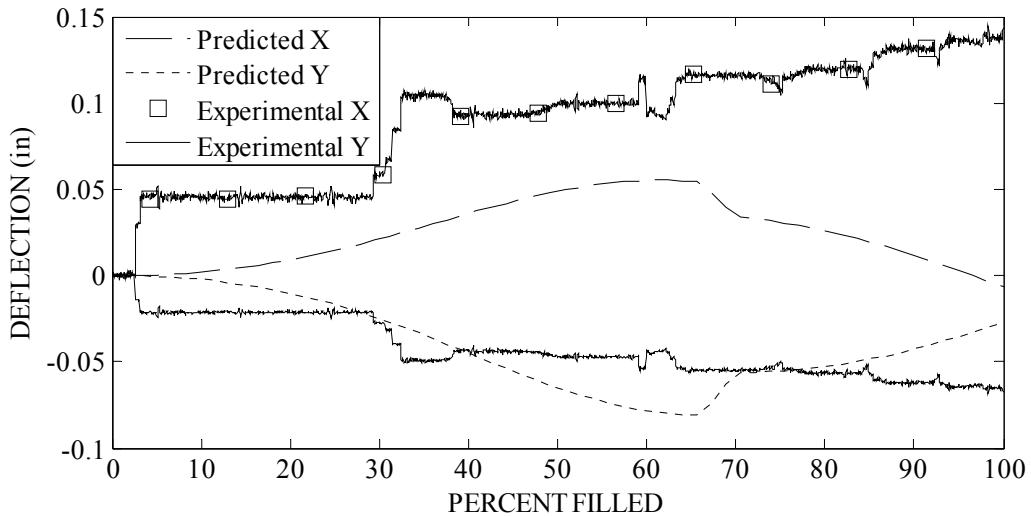


Figure 16. Left Shoulder Displacement, Model and Laboratory

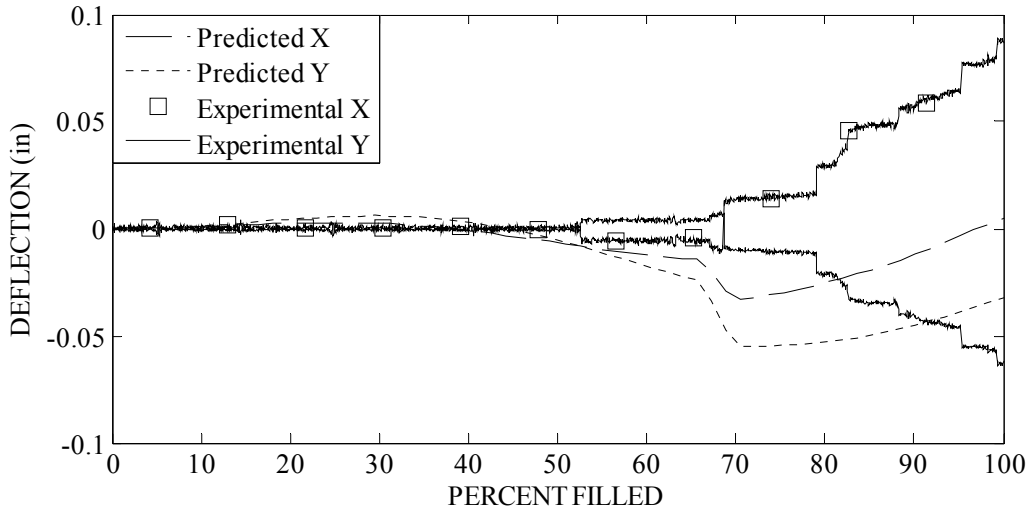


Figure 17. Right Shoulder Displacement, Model and Laboratory

Global displacement results do not match the model. Peak positive displacement at the apex was well modeled, but the final displacement at the apex was almost three times the estimate, suggesting that the structure was less stiff than modeled, either through additional support rotation, a lower elastic modulus, or possible subsidence of a support. A similar result can be seen in the shoulder displacements. The left shoulder displacement follows the proper direction for the first half of the test, but instead of the shoulder returning close to its original position, as predicted by the model, the shoulder moved further right (positive x direction) and further down (negative y direction). The right shoulder did not match predictions. Displacements start out very small, as predicted, but when displacements become larger the x displacements goes from slightly negative to positive, meaning that it was moving right instead of left. The y-displacement at this shoulder becomes more negative, but only in the phase when it was supposed to become less negative. The entire arch shifted right and down compared to the predicted value, an assessment consistent with movement at the right footing.

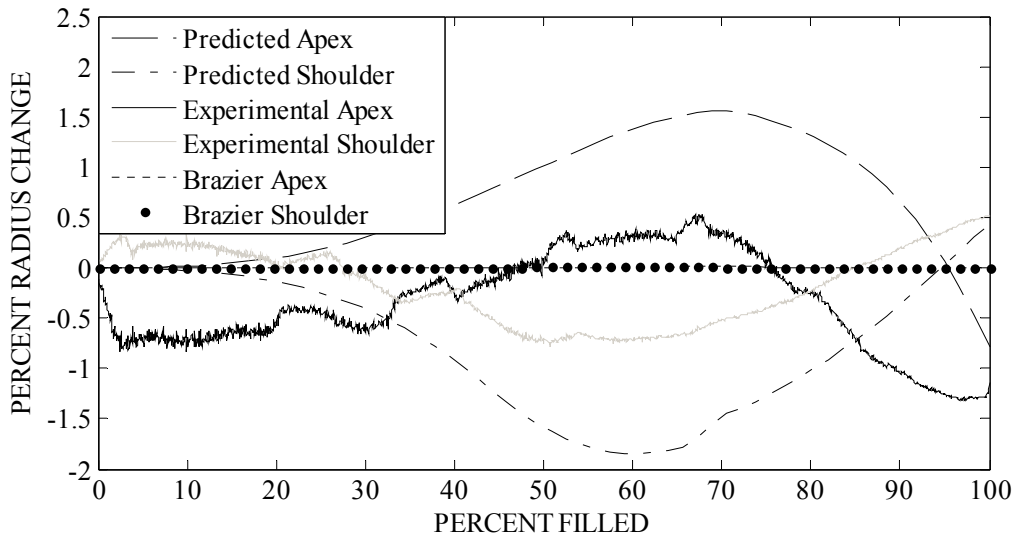


Figure 18. Ovalization, Model, Laboratory, and Without Arch Curvature

The model shows some valuable insight when predicting the ovalization. As proposed, the arch ovals based on bending curvature (from moment) and total curvature (including the curvature of the arch). Initial ovalization is poor because the surplus concrete pooling at the apex was not considered in this analysis. Additionally when the section is partially filled with concrete the model poorly predicts ovalization because the shell warping effect of partial concrete load may be larger than the shell warping from ovalization. Usefully, the final ovalization was well predicted by the model, and the ovalization from the point where the shoulder became fully filled (65% filled) until 100% filled was the closest portion of the model. Change in ovalization as a function of moment was displayed during the test, both gauges change sign of ovalization, as indicated by the model.

Using the Brazier equations as initially written indicates little ovalization, always negative, as they depend on bending stress squared, a positive and very small quantity, instead of bending stress and total stress which is much larger and can potentially have different signs. Figure 18 also shows Brazier’s effect with the unmodified equation for beams, notice that the Brazier bending curvature for both the apex and the shoulder is essentially zero for the entire test; this is a much worse prediction than the modified equation which tracks the positive and negative changes as well as capturing final magnitude.

Field Fill



Figure 19. Belfast Bridge during Arch Fill

Test Setup

Sixteen arches were cast in place over the Little River in Belfast, Maine for a bridge constructed autumn, 2011. Figure 20 contains a section view of the bridge with instrumented arches darkened. Arches were connected with FRP decking prior to concrete filling giving additional restraint to out of plane motion compared to the arch in the lab. In the field, arches were cast into two continuous reinforced-concrete footings. The footings were placed against bedrock, and under the relatively low concrete filling loads it is assumed that the footings neither displaced nor rotated – they are modeled as fixed boundaries. Additional loads were present on the arches, as several people were on the arches as they were filling. While their load is distributed across multiple arches, it is likely that their load influenced the strain and deflection measurements.

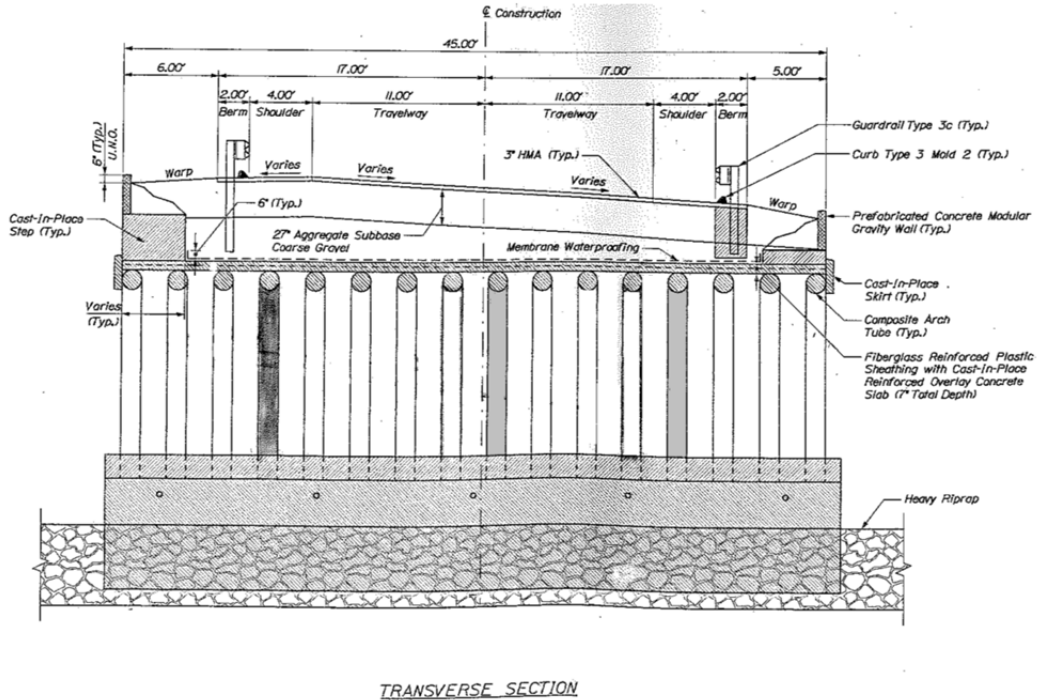


Figure 20. Instrumented (Dark) Arches, Numbered Left to Right

Instrumentation

During filling only selected arches could be instrumented. Only Arch 4 was instrumented for displacements. Measurements were taken at the apex and one shoulder each using a cluster of three string pots capable of measuring all three dimensions of motion. Unfortunately, the string pots were attached to the base of the arch, not the neutral axis, so it is likely that ovalization had an influence on the measured displacements. Also, gauges were mounted on scaffolding approximately 9.84ft above the bed of a flowing stream approximately 3.3ft deep. Large chatter recorded by all string pots was likely caused by flowing water and the unstable platform of the scaffolding.

Arches 4, 9 (mid), and 13 were instrumented with strain gauges. Gauges were installed before the arches were moved to the bridge site with longitudinal gauges on the lower fiber and a second gauge longitudinal, 45 degrees around the cross section from the top fiber of the arch to prevent interference from the decking. Gauges were installed at three locations along the length of each arch – at the footing, shoulder, and the apex. The footing had an additional horizontal gauge to measure hoop strain. Some of the gauges did not function during the fill test. There was no way to reach the shoulder-mounted gauges on Arches 9 and 13, so only footing and apex strain were measured. Also, some gauges had become disconnected or registered no voltage the day of filling, and there was no opportunity to replace the affected gauges.

Results

As with the laboratory results, all of the following plots show the actual field strain and displacement without any attempt to average the data or reduce the error in the instrumentation. Field results were more irregular than laboratory results; the difference from the model is greater in most circumstances and the instruments show a less precise answer displaying significant oscillations in the data. For deflection, this was probably caused by having an unstable platform. Deflections were measured from scaffolding in a flowing stream, and the current would cause sway capable of affecting the small deflections observed during testing. Strains should have produced smaller oscillations as the gauges were mounted to the arches, which should have been stable, but they also showed large fluctuations over small time intervals, not indicating a change in strain but indicating uncertainty in the measurement.

Strains are reported separately for all three instrumented arches, as it is difficult to distinguish multiple plots on the same graph. Gauges from arch 4 appear as a bolder line type, but they actually just have a smaller time step, 0.2s between samples instead of 1.0s. Oscillations in the strain data may have been caused by vibration in the arch, but it is more likely that it was an artifact of the test and originates from an inconsistent voltage source or similar problem instead of a mechanical event. In total there are seven strain plots; all three arches had at least one strain gauge ‘functioning’ at the apex and footing. Gauges that are not reported recorded an amount of strain consistent with a disconnected wire, meaning that the gauge had been damaged by river flooding prior to testing. Typically, damage occurred in the footing gauges; two longitudinal gauges were disconnected at the footing. As the strain gauges at the shoulder of arches 9 and 13 were unreachable, no data is present for these samples. On Arch 4, only one gauge at the shoulder recorded strain, the other read a constant strain throughout the test and was omitted from results, as the gauge must have been partially disconnected from the arch. When arch 4 was filled the pump truck was stopped for a time and refilled after running out of concrete; an attempt was made to remove the data recorded during this time so that percent filled would match up with predictions. Strain at each location for the instrumented arches is in Figure 21 through Figure 27.

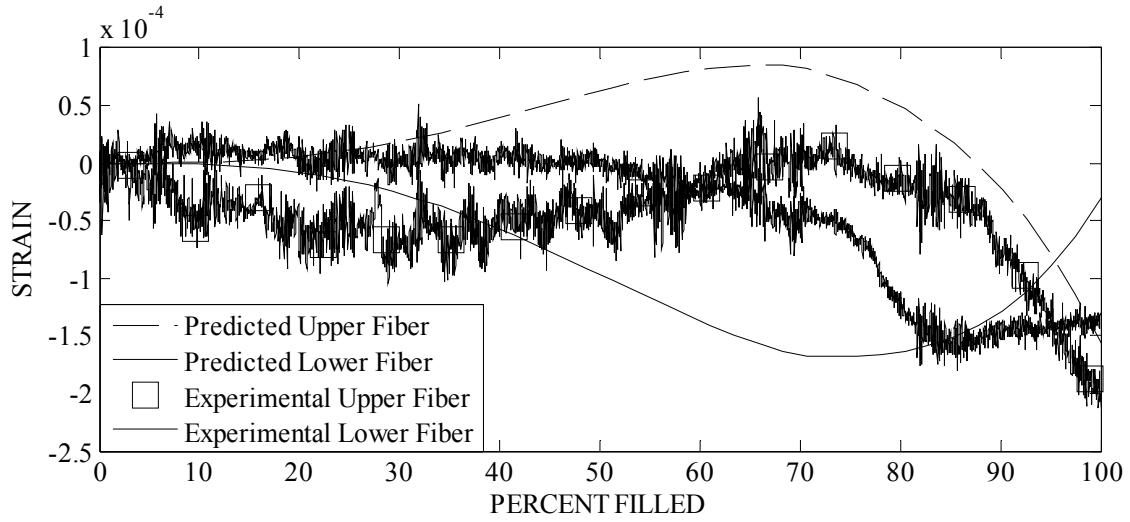


Figure 21. Apex Strain, Arch 4

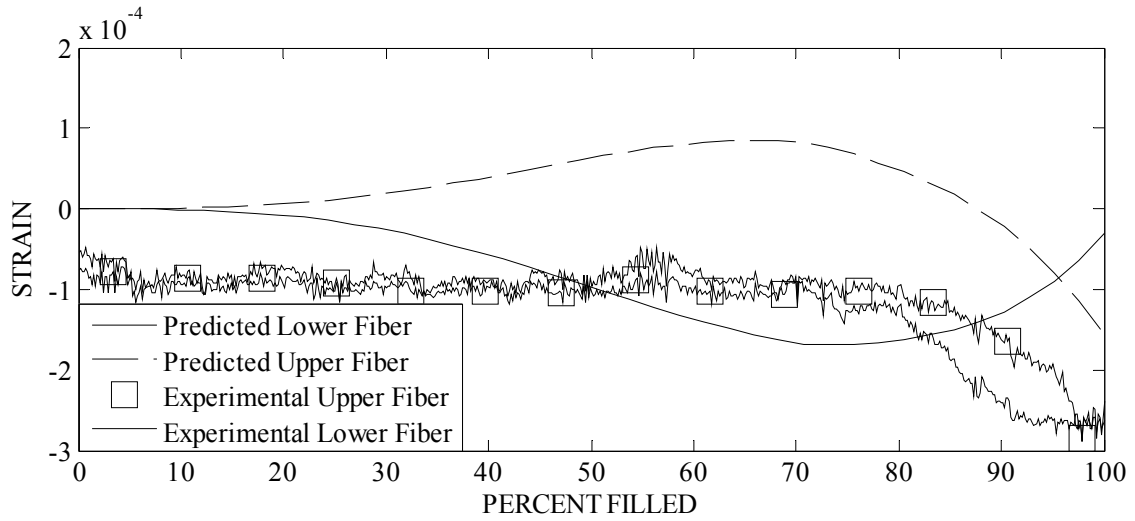


Figure 22. Apex Strain, Arch 9

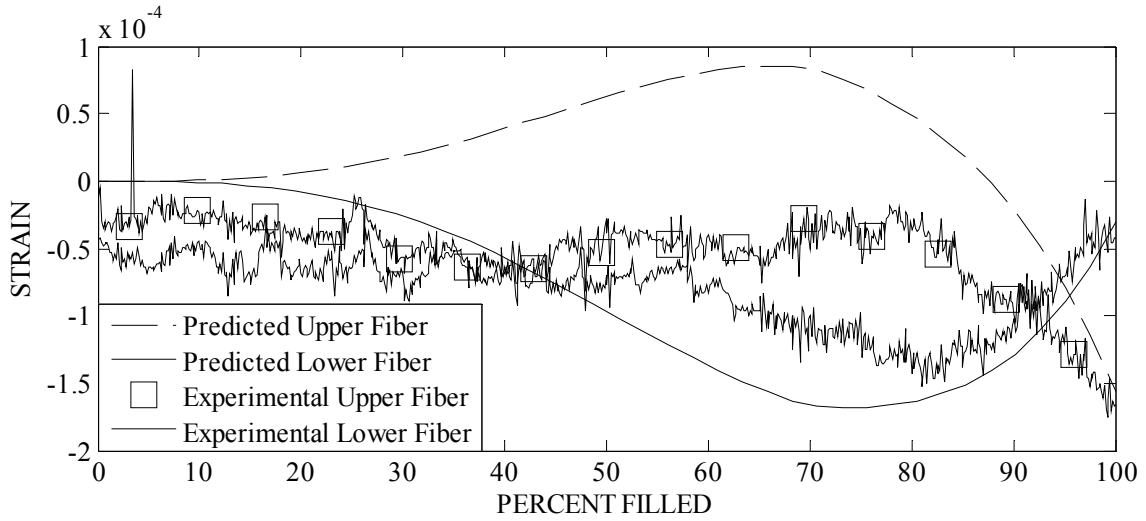


Figure 23. Apex Strain, Arch 13

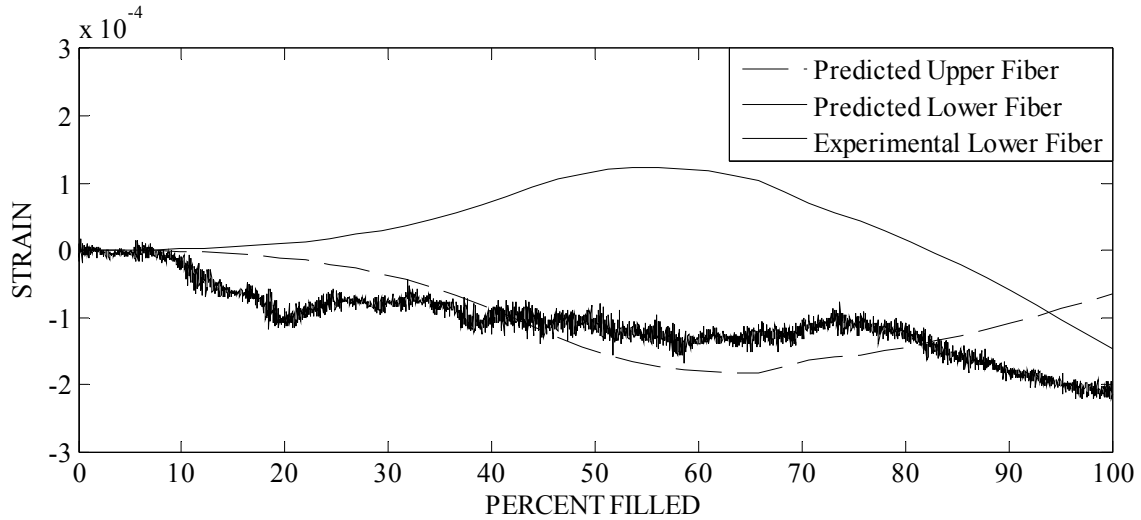


Figure 24. Shoulder Strain, Arch 4

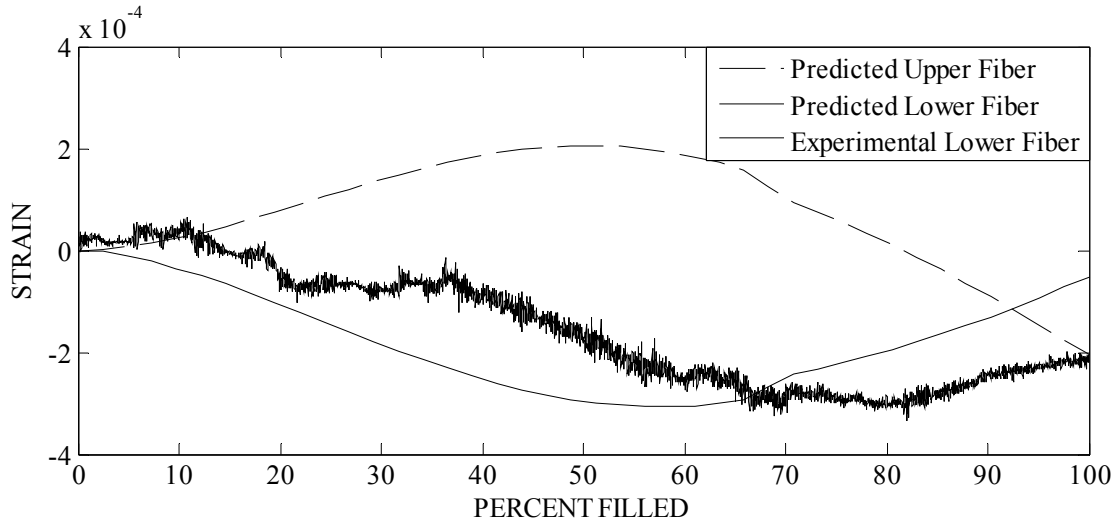


Figure 25. Footing Strain, Arch 4

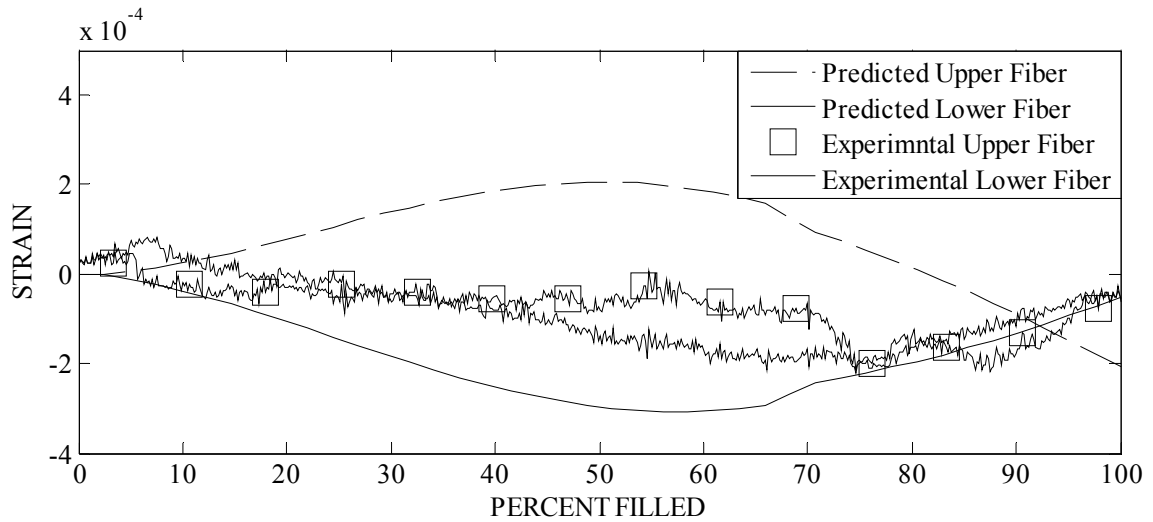


Figure 26. Footing Strain, Arch 9

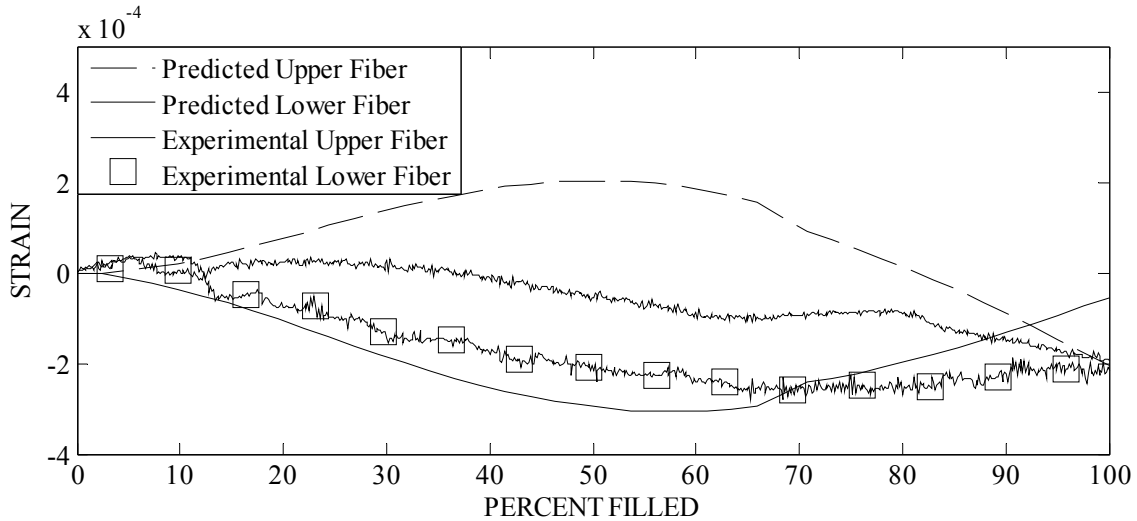


Figure 27. Footing Strain, Arch 13

Strains recorded during filling did not closely match the model predictions, the laboratory loads, or each other from arch to arch. Once again, strain at the apex was closer to predictions than strain at the footing. No information came from strain at the shoulder as the only functioning gauge did not compare well to either the expected top or bottom fiber strain. Strain at the apex showed, for arches 4 and 13, a final strain close to expectation, and the apex strain for all three arches showed a change in moment in the final 10% of filling. The footing gauges were so different from expected loads and each other that it is difficult to draw conclusions from this test.

Deflection measurements were much better than strain measurements. Measured only on arch 4, deflection graphs still show a poor correspondence between the model and field results, but trends and ultimate magnitudes are closer than for strains, and may be closer than laboratory results. Arch 4 deflections and model predictions appear in Figure 28 and Figure 29.

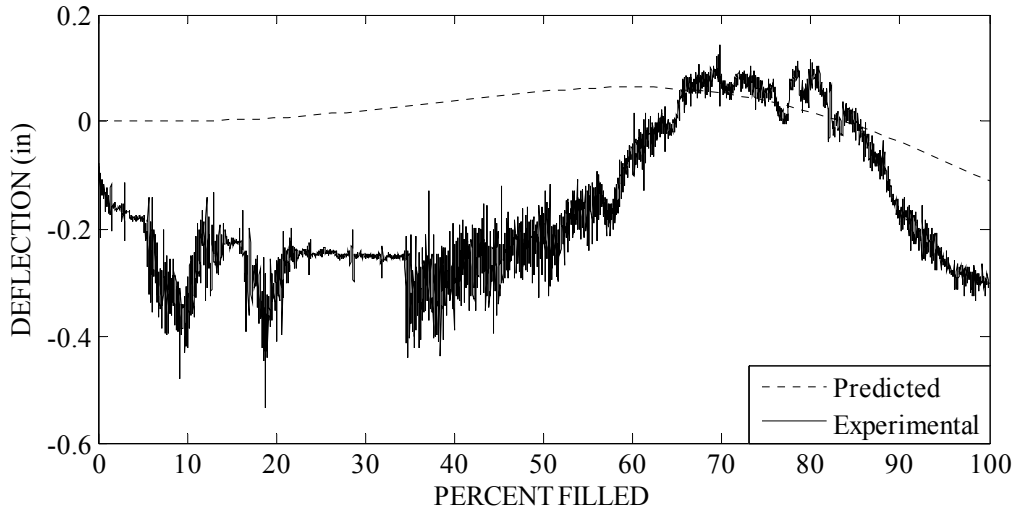


Figure 28. Apex Displacement, Arch 4

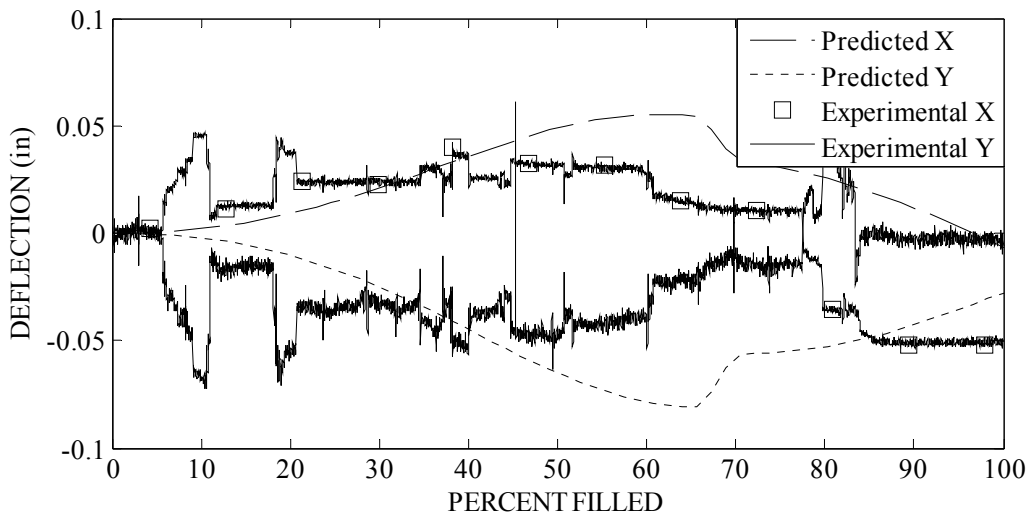


Figure 29. Shoulder Displacement, Arch 4

Displacement at the apex of arch 4 shows decent correlation with the peak and final displacements, better in fact than laboratory results. This was probably because the supports were fixed, as modeled, and there was very little opportunity for support rotation. It was unfortunate that arch 4, the best-instrumented arch, did not have a continuous pour; the operations halted while the pump truck was refilled. Data was removed from the recorded time on the site that the truck was not pumping, but it is possible that there was additional down time after the truck was in position. This may explain the flat spot between 20% and 30% full on all graphs from arch 4; it would also

stretch the remainder of the graph making the peak displacement duration closer to the predicted. The initial negative phase at the apex was a larger magnitude than anticipated by the model. This may have been caused by additional dead load from people and equipment (the arch deflection at time 0 is not 0in) or a more viscous concrete than that used in the lab that tended to stick to the arch more and disrupt the assumption of uniform fluid height used in the model. The shoulder displacement shows the correct sign and order of magnitude for displacement for the middle portion of the fill, but the trend was very different and the final displacement was different from predicted.

Conclusions

Experimental results for strain and displacement did not match as closely to models as desired. One exception was the apex strain, which had good results in the laboratory and slightly better results than the other strains in the field. Apex strain is, in all arches so far tested, the critical strain for apex loading because the apex has reduced capacity from the hole drilled for concrete filling. Strains measured at the shoulder and the footing were typically lower than the model prediction.

At this time, the test and model results indicate that the arches are manufactured with a considerable factor of safety against failure. UMaine looked at the Caribou Bridge as a case study. The Caribou Bridge has an estimated factor of safety of 2.7 against buckling during filling. However, the factor of safety decreases rapidly with geometry change. The Caribou Bridge is a slightly flatter and less than 15% longer bridge than Belfast, yet the peak stress is about twice as high. Also, though not reported, the ovalization should be approximately twice as high (as both stress and ovalization are close to linear with respect to moment) and ovalization may have reached a point where there is a noticeable decrease in section modulus. Beam testing indicated that ovalization was insignificant because the failure moment was so far below the predicted moment that very little section would be lost before collapse. The modified ovalization equation, when coupled with the modeling and confirmed by the laboratory filling test show that measurable, significant, ovalization can occur at lower moments for arches because the bending stress acts through the large arch curvature instead of the small bending only curvature of an initially straight beam. Furthermore, the sign of the ovalization is going to depend on the sign of the moment, meaning that at some potentially critical locations (moment of the shoulder when fully filled) ovalization will actually elongate the section, reducing the bending stress. Unfortunately, the critical stress at the apex will also have a reduced section under the final load, meaning that stresses will be higher at the apex from the same moment.

Task 1.2 Improvements to manufacturing process

As longer span CFRP bridges are designed, larger diameter tubes need to be manufactured. Though the basic process is the same there are some technical challenges that need to be addressed. These challenges are highlighted here and in the future it is expected the manufacturing company to address these challenges as even larger diameters are used in design.

The moment capacity of concrete filled braided FRP tubes increases with approximately the diameter cubed, or approximately linearly with longitudinal structural layer wall thickness (up to the point where the failure mode shifts away from tensile rupture of the FRP). An increase in the number of tubes increases moment capacity linearly with cost. The material cost of increasing wall thickness is roughly linear, but the labor cost of significantly increasing wall thickness (by the use of additional layers) grows faster than the relative material cost because of the difficulty associated with fabricating tubes with additional layers. Increasing the longitudinal structural layer fiber orientation angle by 1 degree decreases the arch capacity by roughly 20%. Thus, within practical limits (such as those imposed by decking clear span limits, etc), increases in moment capacity are most efficiently effected through increases in diameter which either decrease, or do not increase the fiber angle. For longer span arches, the optimum diameter becomes larger. There are, however, limits on maximum diameter within the realm of small volume manufacturing practicality.

Challenges to Manufacturing Larger Diameters

Flow Media

Flow media provides the resin with a defined and consistent flow path, allowing the resin to travel rapidly at a uniform rate along a controlled path through the part. Without flow media, the resin would flow at an extremely slow rate and fail to cover all parts completely and evenly. The flow media functions can be achieved using texture on the outside of a reusable inner bladder. These reusable inner bladders can be used for 300-800 parts given proper handling, which makes them very cost effective on a per part basis. However, the up-front cost of each size is currently prohibitive for a small number of initial bridges. The disposable separate component which produces the required flow paths and inner texture is currently made from polyethylene in a co-rotating die molding process. Delstar, a supplier of the tubular HDPE packaging material used in this process as flow media, is constrained by maximum diameter and volume of material per continuous run. Diameters are set by very expensive dies, but material produced by one die size can be stretched to fit a range of diameters. The largest die currently used by Delstar will accommodate 11.5 to 14.5 in. diameter parts. The largest part that can currently be made using this material would have a 14.5 in. diameter and be 130 ft long. Through mechanical and manufacturing tests, this material has been found acceptable in pattern and spacing, though a deeper pattern and smaller spacing would be theoretically better, and the larger end of that diameter range has proven to dramatically increase the fabrication difficulty. Other suppliers, e.g. Conwed Plastics and MoCap Inc., have dies in storage that can produce larger diameters. Both have significantly larger cell sizes than is ideal. AEWc worked with Conwed Plastics to put their largest die, which was previously in long-term storage back into use. The material made with this die can be used to make 15 in. through approximately 25 in. diameter arches. The Conwed Plastics product has a good pattern (slightly deeper than the Delstar product), but very large (~3/4" depending on use diameter) cell size. An example of flow media and cell size can

be seen in Figure 30. This is not ideal for flow or texture, but has been found to be acceptable by AIT. There is a maximum length that the flow media can be produced at for a given diameter, and reduces at an increasing rate as the use diameter increases. Kenway has shown that splicing the flow media together has worked for specimens as needed.



Figure 30. Example of flow media

Delstar can produce a new die at any desired diameter, with any cell sizing and depth, but the cost is on the order of \$30,000 just for the die, and not including setting up a new machine run. Given the difficulties experienced with using the material from existing dies at the extremity of their working diameter ranges, the cost of a new die is potentially justifiable.

Braided Fabric

The braided fabric, although fairly simple in its finished form, has many interacting parameters affecting possible configurations. These include: braid angle, number of tows or rovings, tube diameter, tension and compression jam angles, maximum length, crimp angle and minimum radius of curvature. Each of these is discussed below along with their implications on each other. Afterwards, the two braided fabric layers are discussed individually.

Braid Angle

The braid angle refers to the angle between the longitudinal axis of the tube and the tows, or rovings. Reducing the braid angle increases the longitudinal strength and stiffness of the braid and reduces the hoop strength and stiffness. For a given braided tube, the braid angle and diameter are intrinsically linked in that as the tube is ‘pulled down’, the braid angle decreases at the same time as the diameter. The limits of minimum and maximum braid angle achievable by a given piece of braided tube are known as the tensile and compression jam angles, respectively. The jam angles not only define the minimum and maximum tube diameters, but the minimum achievable radius of curvature for a given diameter. This technology exploits the consistency of the compression jam angle to provide a consistent diameter along the section length of an arch and among arches of the same construction. The diameter constraining layer provides this consistency, as well as efficiently reinforcing the arch in the hoop direction. Maximum structural efficiency then comes with longitudinal structural layers which are oriented as

far in the longitudinal direction as possible, with a ~20% increase in tensile strength for each degree more longitudinal the orientation can be made. Thus increases in diameter must preserve or reduce LSL braid angle in order to represent a material efficiency gain.

Number of Carriers

The number of starts (or ends) refers to the number of fiber bundles to be braided. A start is supported by a carrier on a braiding machine. In order to achieve the level of consistency required for CFRP applications, each carrier on the machine must have a start. Therefore, the number of carriers on a machine defines the number of starts. Figure 31 shows a simple 50-carrier machine used in the manufacturing of braided materials. This particular machine is used to braid ropes, but the basic function and structure is similar.

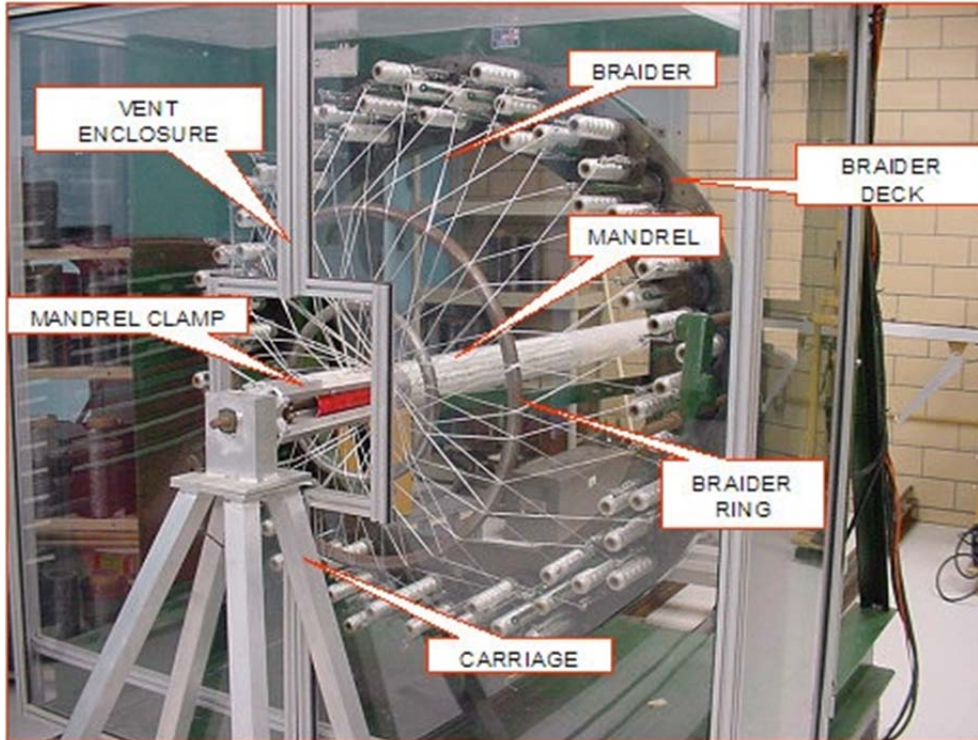


Figure 31. Rope Braiding Machine

Available Equipment

A&P Technology, located in Cincinnati, Ohio, is a world-leading producer of precision braided textiles. They have world’s largest and most technologically advanced braiding machinery to make large diameter braided fabrics with small and large unit cells. The company owns a variety of braiding machines each designed to use a specific number of carriers, ranging up to 800. More carriers allow for larger diameters with greater coverage and layer thickness. That is, if a 400-carrier machine can make an 8 in. compression jam diameter braid, then a 600-carrier machine will make a 12 in. compression jam diameter braid with all other parameters being equal. If there is no machine size between those two, it will be difficult or impossible to produce a braid

between those sizes without either building a new machine at substantial cost, or making changes to one of the other parameters, such as reduced area weight or increased tension jam diameter. Some of these changes might significantly reduce the structural capacity or usefulness of the braid. It is possible to produce structurally efficient braid angles for braided CFRP tubes with diameters up to 25 in. and layer thickness of approximately 0.06 in. using the 800-carrier machine and very heavy tows. Even larger diameters are possible if compromises are made to desired coverage, braid angle, or part thickness, or if a larger braiding machine is constructed. Useful braids for CFRP as small as 6 in. diameter have been manufactured.

Diameter

Increasing diameter can be done stepwise by using a bigger machine. The need to fine tune the diameter within these steps must be balanced with 1) the extra cost of additional ends per carrier or twisted tows, 2) the structural impact of varying the fiber angle and thickness of the braid, and 3) the structural impact of increased diameter variability. Smaller tows can reorient more before compression jam, resulting in a larger compression jam diameter. The opposite is true of larger tows. However, larger tows result in a thicker layer, while smaller tows result in a thinner layer. Using two tows per carrier reduces the compression jam angle slightly in comparison to one tow twice as big per carrier. This is because two tows per carrier also result in flatter fiber bundles compressed together that lock at a lower angle. For an additional cost, the roving making up each tow can be twisted, making the bundle of fibers more rounded and allowing more reorientation to higher angles before compression jam, with minimal impact on final structural properties. Since the further from the hoop direction the more a small change in the angle results in a larger change in diameter, any change resulting in a lower fiber angle (further from the hoop direction) magnifies variability from other sources, such as uneven elastic tension, throughout the length of the fabric.

Additional Interaction of Braid Geometry Parameters

Allowable curvature is increased by increasing the braid angle, which reduces its structural efficiency. The minimum bend radius can be also reduced by decreasing the number of carriers and/or the number of fibers per carrier, which reduces the tensile jam angle. This also reduces the total amount of fabric, which thereby reduces the overall strength and stiffness of the part. Layer thickness can be increased by increasing the number of tows or tow size, but both changes increase the tensile jam angle. Increasing the tensile jam angle lowers strength and stiffness and increases the minimum radius of curvature. Thicker tows and more frequent crossings (higher pick count) also result in a larger crimp angle, which results in a slight reduction in structural properties. For a single layer, using less material at a lower braid angle provides better structural efficiency than using more material at a higher angle. Thicker layers are more efficient than multiple thin layers because while material cost is doubled, braiding costs do not. This is expected to far outweigh the efficiency losses due to the increased crimp angle.

Diameter Constraint Layer (DCL)

The Diameter Constraint Layer (DCL) provides a consistent diameter and strength and stiffness in the hoop direction for the braided FRP tube. The DCL provides a consistent diameter by reorienting to higher angles until it can reorient no further, reaching the point of compression jam. Two important characteristics of the DCL for FRP manufacturing are a consistent compression jam angle and the hoop stiffness and strength. The former is necessary for a part to have constant diameter, and the latter provides the required confinement of the compression carrying concrete when the filled tube is subjected to bending.

Longitudinal Structural Layer (LSL)

The longitudinal structural layer (LSL) is a biaxial braided fabric with a braid angle under 30 degrees. In order to efficiently resist the tensile and compression loads due to bending moments in braided FRP tubes, the LSL is oriented as close to the longitudinal direction as possible, while still allowing conformability to the range of desired curvatures. The LSL should never be at tensile or compression jam angle in use, as it needs to conform to the required curvature of the part.

The maximum structurally optimized LSL that has been designed to date has a diameter of 25.5 in., but larger diameters are possible with compromises in layer thickness and/or fiber angle. For a 25.5 in. diameter and 0.060 in. thick LSL, the maximum continuous length that can be produced is approximately 205 ft. Although costly, retrofitting the braiding machine with larger carriers can increase the maximum continuous length. Longer parts could also be made by using more, but thinner layers.

What to Manufacture

AEWC has learned that A&P is currently limited to approximately 25 in. diameters while maintaining the present hoop strength and stiffness. Diameters larger than that with existing equipment require thinner layers, inefficient constraint layer braid angles, or compromises to the plan view geometry flexibility of the arches. A thinner constraint layer or inefficient constraint layer braid angle will both reduce strength and stiffness in the hoop direction. Lower hoop capacity is undesirable and other options should be explored as arch capacity can be driven by a lack of confinement in the concrete leading to concrete compression failure. It is believed that there already exists a reduced level of confinement in the larger 15" diameter tubes, which increases the potential for concrete compression failure.

AEWC has investigated using an inherently higher capacity material such as carbon for the diameter constraining fabric in order to offset the geometric capacity reductions that come with increasing diameter. A&P has performed braid modeling to produce sample braid geometric properties, which AEWC has used to predict moment curvature behavior of arches. Figure 32 shows the moment curvature relationships of three hypothetical configurations of arch. The green curve uses E-glass for the DCL where the other two use different configurations of carbon, otherwise the three hypothetical arches are identical. The glass diameter constraint layer, with its much higher strain to failure,

offers dramatically more ductility, and slightly more ultimate capacity at (roughly approximated) 30% of the cost of the carbon DCL options.

Moment-Curvature for Three Laminate Configurations

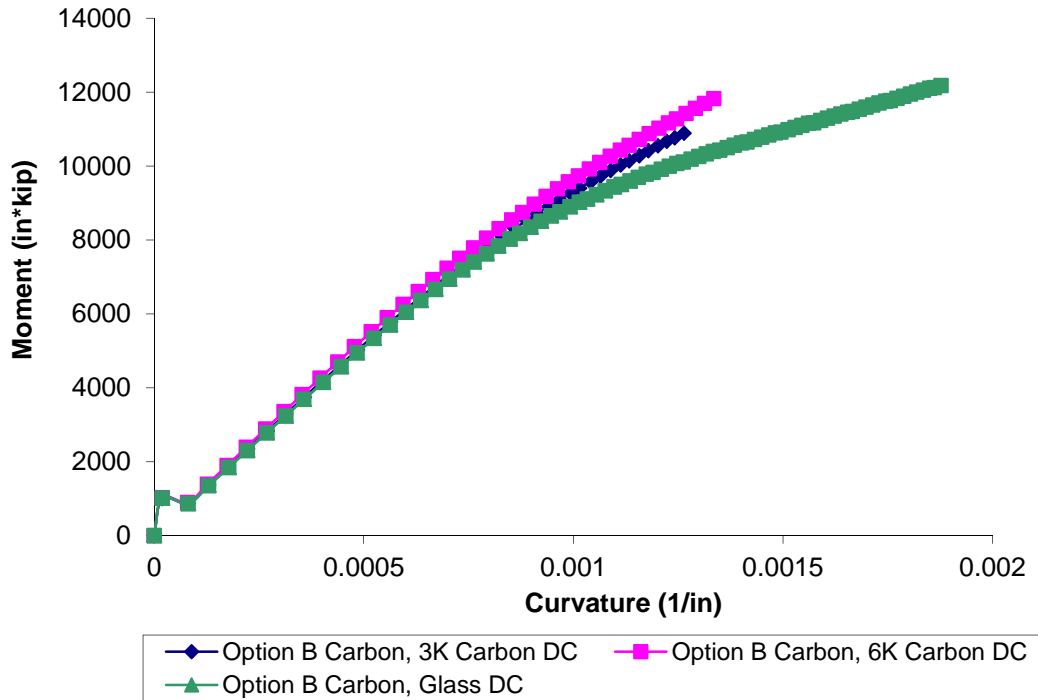


Figure 32

Fabric Quality Control

AEWC has worked with A&P on quality control of the arches. A&P has excellent overall quality control measures in place, but there was room to improve the DCL fabric used in the arches. The issue was a disparity between the attributes for which they control (those which are important to their other customers) and those important to arch construction. For arch construction, since the DCL diameter tolerances are critical to providing adequate formability of the LSL while maintaining the desired moment capacity, DCL diameter tolerances are of extreme importance. Early in the process of improving quality control, A&P determined that one of the primary factors in diameter consistency of the DCL was the type of elastic used for the elastic axial, and the tension in these tows. They made this determination on the basis of the fact that material made without this fabrication aid exhibited their typical higher level of quality. Also, some

orders received by AEWC exhibited excellent diameter uniformity at one end of a run and poor uniformity at the other end.

Examination of their production notes showed that the only un-tracked relevant parameters were elastic type and tension. In a few sample runs, A&P determined that the tension in the low tension elastic axial spools was lowest at the beginning of a run, and highest at the end. Since neither AEWC nor A&P could determine which end of the run was the beginning or the end, A&P ran two short runs of material with one at the lowest possible tension and another at the highest possible tension to compare the effect. They took lay-flat width measurements at six-inch intervals and determined that both runs had excellent consistency. A&P then sent the specimens to AEWC, where we took circumference measurements at six-inch intervals along the length of sample with the sample inflated to 5 PSI. A discrepancy was found between the actual diameter measured by AEWC and the calculated diameter provided by A&P. Further, AEWC found a COV of 0.17 in the high tension specimen and only 0.10 in the low tension specimen. The COV for material from the middle of material left over from a previous run (neither high nor low tension) was 0.03.

Table 4. Fabric Characterization

More Tension	UM 6722	Reduced Tension	UM 6723	Neil Bridge Arch	UM 6447
mean	9.103	mean	8.958	mean	11.725
min	8.525	min	8.650	min	11.650
max	9.375	max	9.200	max	11.800
standard deviation	0.150	standard deviation	0.087	standard deviation	0.035
cov	0.017	cov	0.010	cov	0.003

Exploration if this issue resulted in the conclusion that the lay flat width of the fabric was not a good predictor of the diameter of the inflated arch. AEWC sent A&P a low cost dummy bladder which would approximate the arch inflation process for purposes of checking diameter uniformity. A&P has already realized a significant reduction in COV as a result of this work, and has an important tool for further improvements. Using this new approach A&P also discovered a significant refinement to their prediction software for our application. Since the LSL fiber angle is critical, and the fiber angle depends on diameter, and the diameter is derived from the DCL, not only is low variability about the mean important, but the ability to accurately predict the mean for a new size is also important. Further, the ability to accurately predict the tensile jam angle of the LSL is important to A&P’s braid architecture design process, since lower angles are far more effective, but a braid design that can’t achieve the specified low angle can’t be formed to the required curvature. As can be seen in Figure 33, the jam diameter/angle depends on tension.

UM6718 Tensile Jam

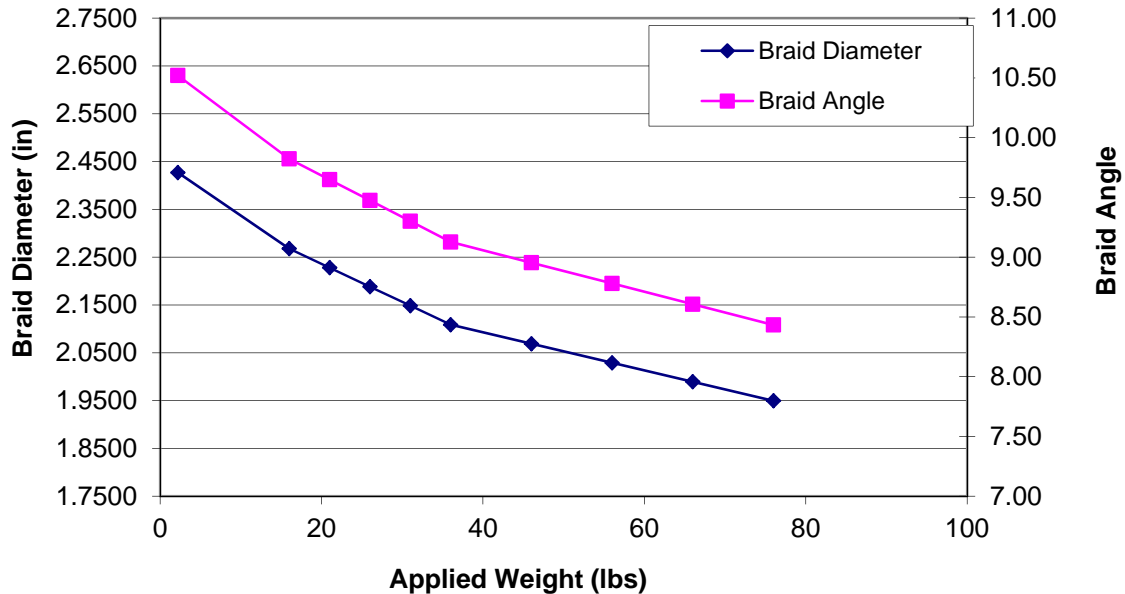


Figure 33

Knowing that the hoop tension equals the pressure times the hoop radius, this angle vs. tension model can significantly refine the accuracy of braid geometry predictive models. The net result is a ~7% improvement in geometric efficiency of the LSL without the cost of having to make trial runs of a new braid. This is important during the early phases of commercialization where rapid turnaround time on new configurations with good accuracy can be critical.

Difficulties in manufacture of larger arches encountered in the spring of 2010:

- Flow media which is near its maximum use diameter is very difficult to properly position.
- Flow media which shortens as it increases in diameter is acceptable as long as it doesn't need to increase diameter significantly. When the base diameter is much smaller than the use diameter, this causes problems with the positioning of the primary flow paths (spiral infusion tubes.)
- The inner bladder material is intolerant to handling roughness. Very small punctures can create a major problem during infusions. The present inner bag

used by AEW C for this process is not a typical vacuum bag film. This is due partly to the large diameter of the tube compared to other similar processes and the required arch shape of the bag. The vacuum bag specific film is manufactured in a similar process as the inner bag, with defects similar to the material used in the arches, but vacuum bagging film is made from two blown films laminated together such that two defects need to coincide – which is highly unlikely – in order to present problems if carefully handled. Vacuum bag specific bags are also more brittle than the bag presently used and require greater control of environmental conditions. Tubular forms of typical bags are not as available as the bag being used.

- Larger end plugs are hard to handle as they weigh much more than the previous 12” diameter plugs. More labor is ultimately required for these plugs to be handled safely during manufacturing.

Task 1.3 Bracing Mechanisms

Bracing mechanisms for this task focused on preventing changes in section shape with restraint to the arches at points of maximum moment. It was anticipated that more robust decking (SuperRail from Creative Pultrusions) and connections would greatly increase the structural stability during construction and be a simple solution to the bracing needs for out of plane movements. Local buckling of the arches and ovalization are still potential problems then as larger sections are used. In Task 1.1 ovalization equations were derived that can be used for design. In parallel with that analytical work, designs for bracing mechanisms was conducted as preliminary analysis showed that ovalization could be a larger problem than it turns out to be for the sizes of arches tested presently. This task will briefly describe the anti-ovalization clamps that were designed and fabricated but not installed during arch filling. As previously mentioned, ovalization was not as significant as initially predicted and these devices were not required for arch filling. It is possible in the future that these could be effective as parts of a bracing scheme or restraint where minor bracing would be more economical than increasing the wall thickness of the tubes. Current designs however do not require this bracing mechanism.

In production, the five required anti-ovaling clamps for the lab filled arch similar to the Perkins Bridge arches are estimated to cost well under \$100 each. This suggested that the discrete anti-ovaling brace approach was worth pursuing further at the time of this work. The moment diagrams for particular load cases show that bending moments change rapidly along the arch. This reduces the number of bracing mechanisms in this scheme.

As can be seen in the filling-load moment envelope for the arches in the Belfast Bridge project in Figure 5 the regions of peak load are often fairly short both during filling and in service, typically with the greatest 10% of the local moment peak within a

4ft span of the arch. This indicates that localized anti-ovalization restraints should be effective at increasing the safety factor without additional structural fiber in the section. That assumes that the influence of the anti-ovaling restraint drops off less rapidly than the typical moment profile when moving away from the local location of peak moment .

Brief tests conducted to determine the magnitude of the region of influence of an anti-ovaling brace showed that the area of influence is significant. In one controlled test to simulate ovalization, the center of a 20 ft long straight section was compressed. The applied load induced ovalization roughly equivalent to the natural ovalization shortening of the minor axis of previous uniformly loaded specimens just prior to buckling. It appears from this testing that the influence area not only extended quite far, but also is of significant magnitude within the region of interest. This test served the purpose of confirming that the approach of discrete anti-ovaling braces has merit. As can be seen in Figure 34 3 ft on either side of an applied ovalization, the section still has half the degree of ovalization applied in the center. Since in most load cases, the maximum moment drops off more rapidly on either side of the peak than the influence of an applied ovalization load (Figure 34), this implies that positively restraining the section against ovalization at one location would provide useful improvement in capacity in that region.

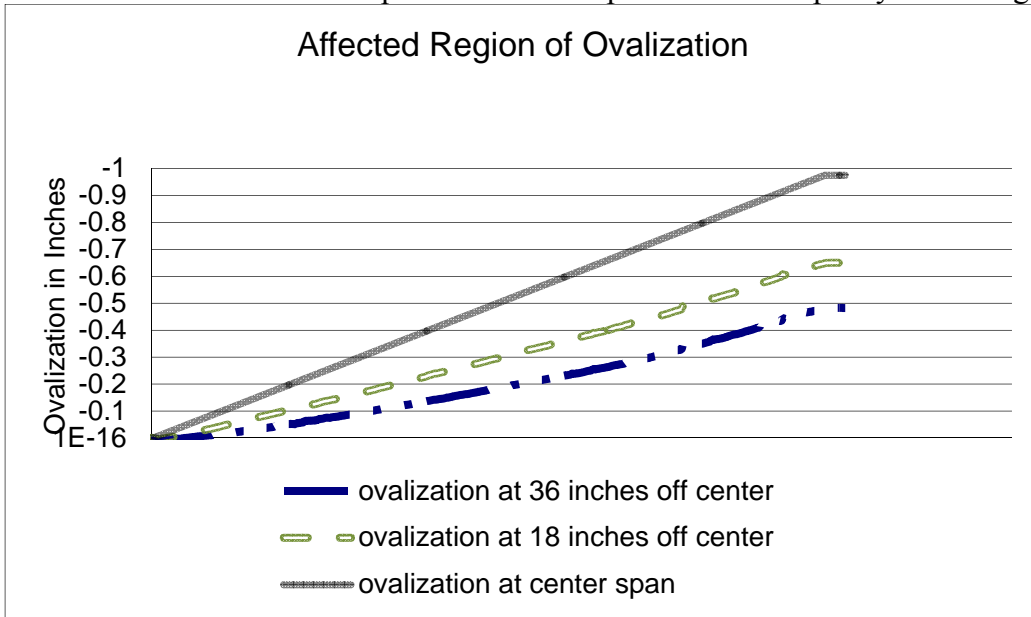


Figure 34. Affected Region of Ovalization

The arch anti-ovaling braces are designed as two-piece circular mild steel I-beam sections that clamp around the circumference of the arch section. These clamp-on braces are bedded in talc thickened polyester resin putty to ensure uniform contact with the arch.

The clamps are 3 inches tall by 3 inches wide, so that they can fit under a single 4 inch by 4 inch corrugation rib of the decking without interference.

Anti-ovalizing clamps were designed and manufactured for use on the 70 foot span arch that was planned to be tested in the laboratory. After design of this bracing, ovalization was shown to be less of a problem than originally expected. The clamps were not used in the laboratory arch fill. Improvements in decking, connections, and engineering analysis have enhanced our understanding of arch behavior during construction, and thus safety during filling.

Arch Testing

Arch testing was completed on a 15” nominal diameter concrete filled glass and carbon FRP tube in the same geometry and layout as the Perkins Bridge in Belfast, Maine. This arch had a span of 47’-7” feet and rise of roughly 11’-0”. The centerline spacing of the pin supports was 51’-2 1/2”. The objective of this test was to validate the model being used for the design of bridges using this technology. This is the first 15” nominal concrete filled CFRP tubular arch tested.

Specimen and Test Setup

An arch fabricated identical as those being used for the Perkins Bridge in Belfast, Maine was used for this test. Samples taken from identical arches for the Perkins Bridge had an average thickness of 0.1362 inches and average FRP longitudinal tensile strength of 126.36 ksi. This arch had a centerline radius of curvature of 31’-3”.

Testing was performed on the structural testing floor at AEW. A 110 kip servo-hydraulic actuator was installed under the floor and connected to the loading fixture at the apex of the arch using DWYIDAG rod. A 12” wide steel reinforced, wooden saddle with 1/4” of neoprene provided a patch load.

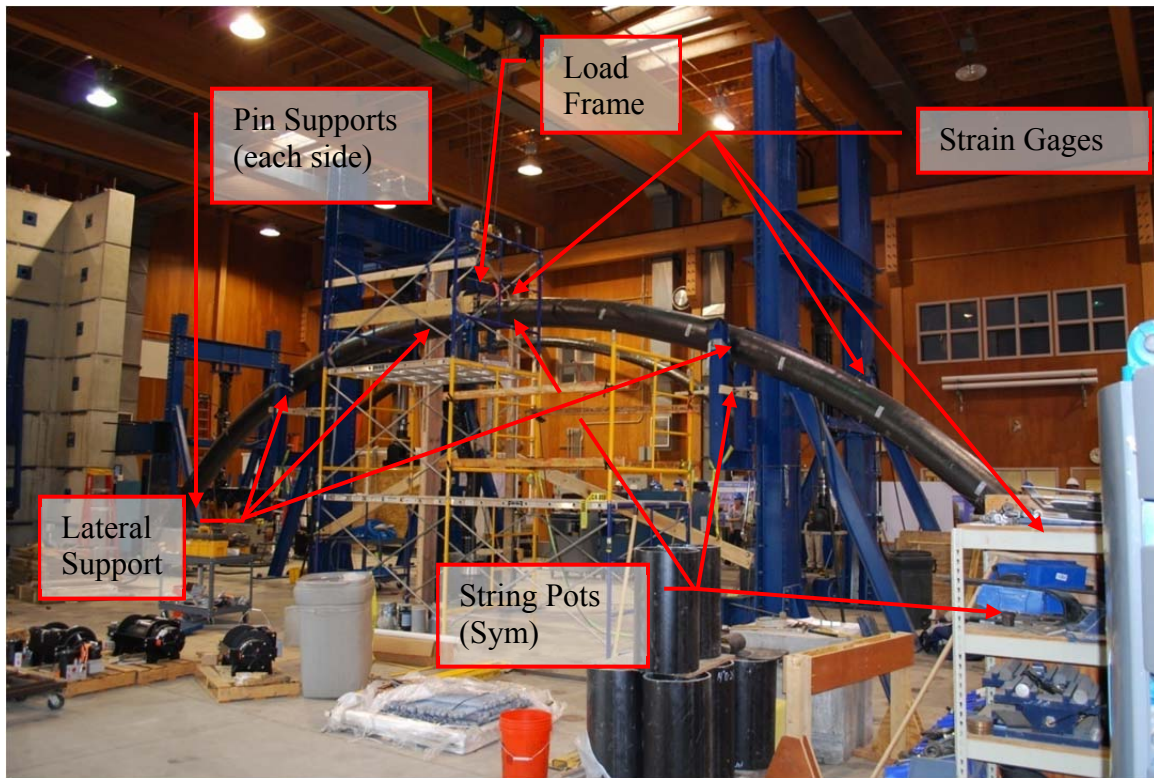


Figure 35. Arch Setup Prior to Failure

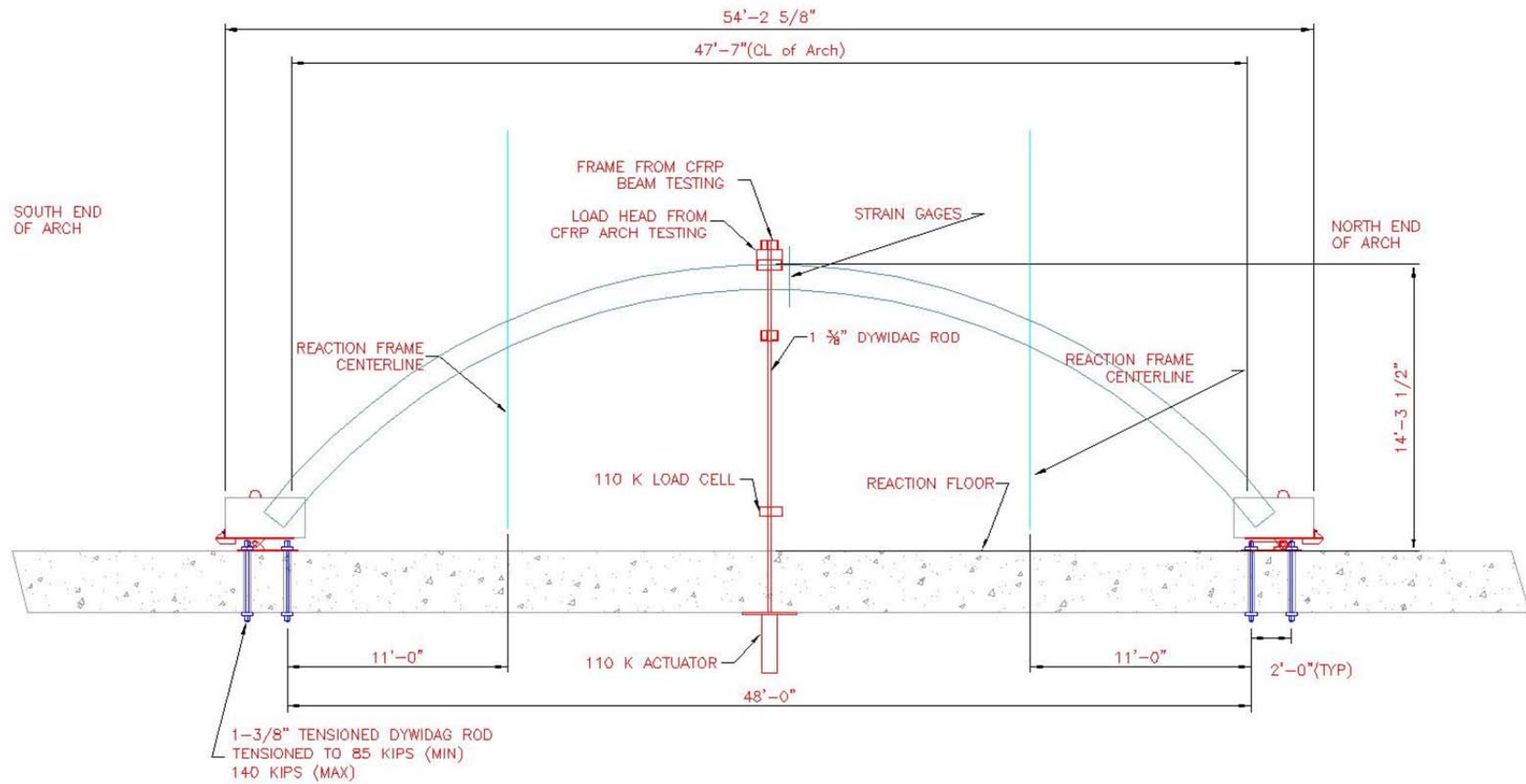


Figure 36. Arch Test Setup

Test parameters (load and deflection) were gathered from a linear RISA analysis.

Instrumentation

Instrumentation during the arch test included foil resistance strain gages, string potentiometers (string pots), and the load cell. Data was collected using National Instruments (NI) data collections systems at 5 Hz.

Strain measurements were made 12” off the apex of the arch, then on the North shoulder of the arch 150 inches from the apex along the arc length of the arch, and at 12” above the North footing. At each (3) cross section, three longitudinal strain gages were placed at the top, bottom, and 45° from the centerline of the arch. Additionally, at the base of the arch, a strain gage in the hoop direction was placed to monitor hoop strain in the composite.

String pots were used at each footing to measure footing rotation, at each lateral support on the shoulders, and at the apex. The setup for these measurements can be seen in Figure 35 through Figure 39. Basic geometry was used to calculate vertical and horizontal deflections at these points. Lateral supports were provided to minimize out of plane movements.

String potentiometers can be seen on Figure 37, Figure 38 and Figure 39. They show the gages for measurements at the apex of the arch, shoulder and footing respectively.



Figure 37. String Pot Measurements at Apex

Three string potentiometers were used at the apex. Two measured vertical deflections and was placed to measure out



Figure 38. String Pot Measurements at Shoulder

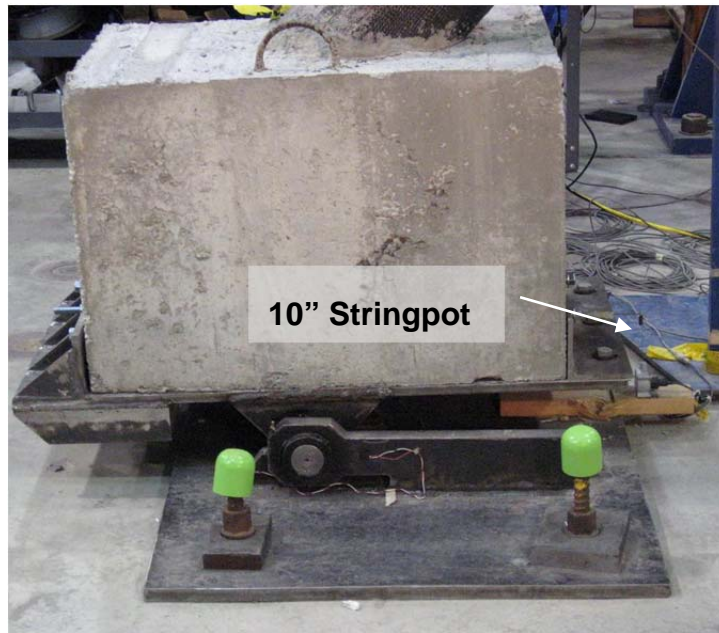


Figure 39. String Pot to Measure Base Rotation



Arch Modeling

Modeling of the filled and cured arch was performed using three different analysis tools. A simple linear RISA model was used for initial calculation of the forces (moment, shear, and axial) in the arch. The moment, shear, and axial capacities were calculated using the draft AASHTO guide specification (Fam, et al 2010) on concrete filled FRP tubes. Input values to this analysis are shown in Table 5. The axial load found in a RISA calculation was one input into the capacity calculation as the axial force affects the moment capacity of the section.

Table 5. Input Values for Section Moment Capacity

Tube Diameter	14.8 in
FRP Thickness	0.116 in
Concrete Strength	6.0 ksi
Allowable Concrete Strain	0.00657
FRP Long. MOE	8680 ksi
FRP Hoop MOE	2644.0 ksi
FRP Ultimate Tensile Strain	0.01570
FRP Ultimate Compressive Strain	0.01200
FRP Poisson's Ratio	0.452
Axial Load	54.5 kip

A nonlinear finite element beam analysis was used to prediction forces in the arch and deflections. Bending failure due to FRP tensile rupture was predicted at a moment of 3000 kip-inches. This corresponded to a total patch load at the crown of 72.1 kips in addition to the dead load of approximately 171 pounds per foot of arc length along the arch.

The axial and moment capacity interaction diagram is shown in Figure 40. This shows the simplified method from Fam (2010) where the interaction diagram is produced using a bilinear curve using pure bending, pure compression, and the balanced compression and bending capacities. It can be seen that the arch failure in the lab is dominated by the bending capacity of the arch. The failure point is slightly inside of the curve and not on the line as expected.

The moment-curvature plots used in the nonlinear finite element model are also shown in Figure 41. As shown in Figure 41, there is very little effect on the ultimate bending capacity of this section with increased axial load. The model takes into account the rotation of the footings and the bearing locations of the supports with a very stiff member to represent the concrete footing. It does not, however, take into the account the unsymmetric rotations that can be seen in the results.

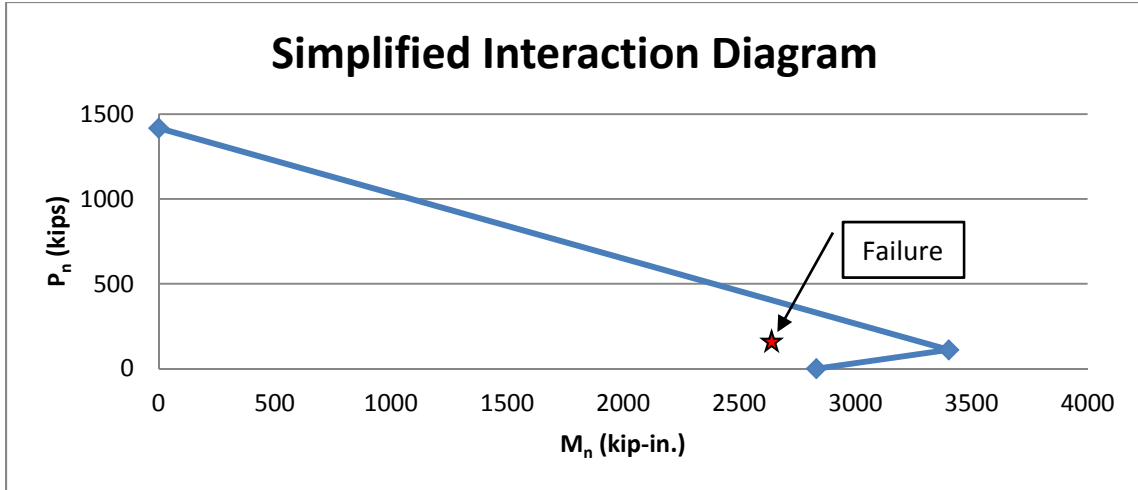


Figure 40

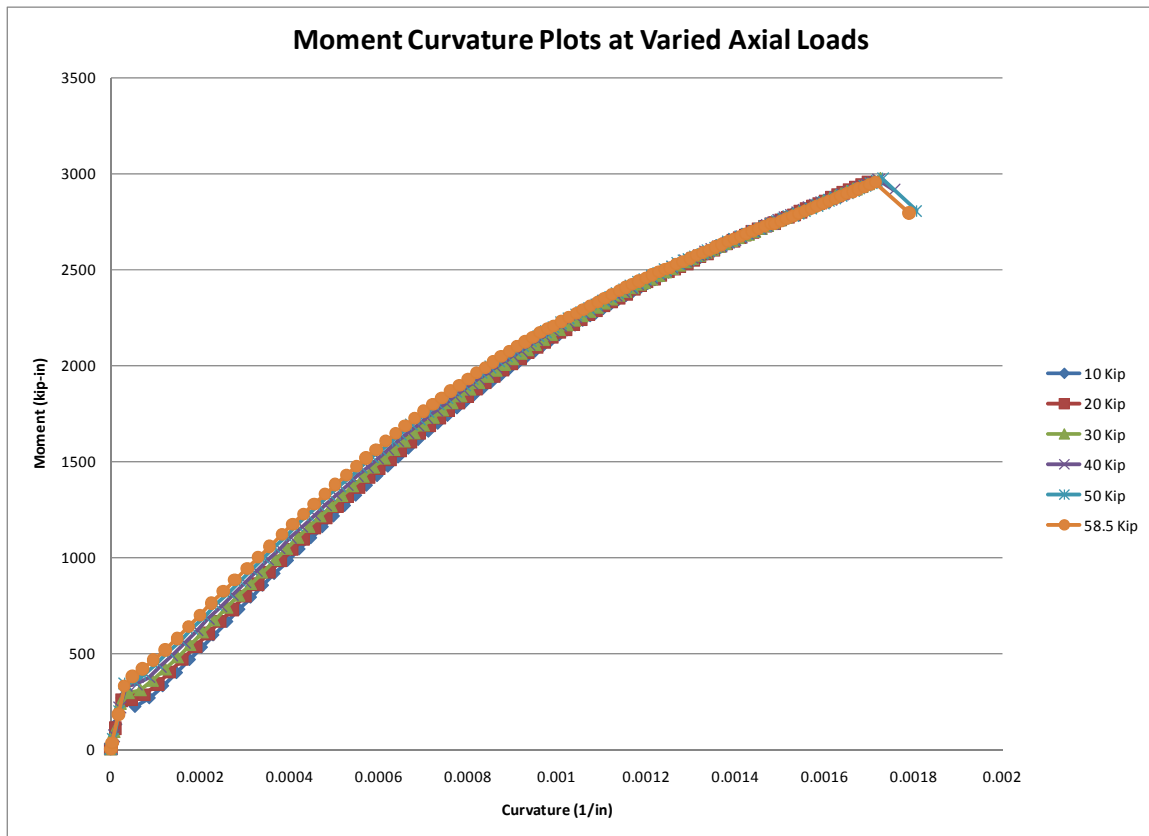


Figure 41. Nonlinear Moment-Curvature Relationships

Results

The arch failed as expected in tensile rupture on the underside of the apex. Ultimate failure corresponded to tensile rupture of the carbon tows in a diamond pattern under the crown of the arch. This can be seen in Figure 42. Several areas of the arch, mainly under

the shoulders of the arches experienced FRP buckling prior to ultimate failure. An example of this can be seen in Figure 43. These areas included the underside of the shoulders and the top of the crown where there was significant compression in the section.



Figure 42. Rupture Fibers of Arch after Failure



Figure 43. Compression Buckling of FRP on Underside of Arch During Test

The load versus vertical deflection at the crown, load versus horizontal and vertical deflections at the shoulders, and load versus support rotation can be seen in Figure 44, Figure 45, Figure 46, and Figure 47 respectively. The shape and peak of the apex load-deflection plot is as expected. The shoulders and support movements show a slight unsymmetric deflection of the arch during loading. This is easily seen in the support rotation plot where the North support rotated roughly 50% more than the South support. The peak load was 70.6 kips and corresponds to a calculated moment of 2626 kip-in. This capacity is 14% below the predicted value of 3000 kip-in. The total vertical deflection during the test at the crown was 10.52 inches. The predicted deflection at a 70 kip crown load was 5.37 inches and the corresponding deflection during the test was 10.29 inches. The model was not run to exactly 70.62 kips. This shows a 47.8% under-prediction during of deflection during the test. As seen in Figure 44, the beginning part of the test which corresponds to the design range of the arches is fairly well represented. This model is not capturing the softening though of the system as the arch gets closer to failure.

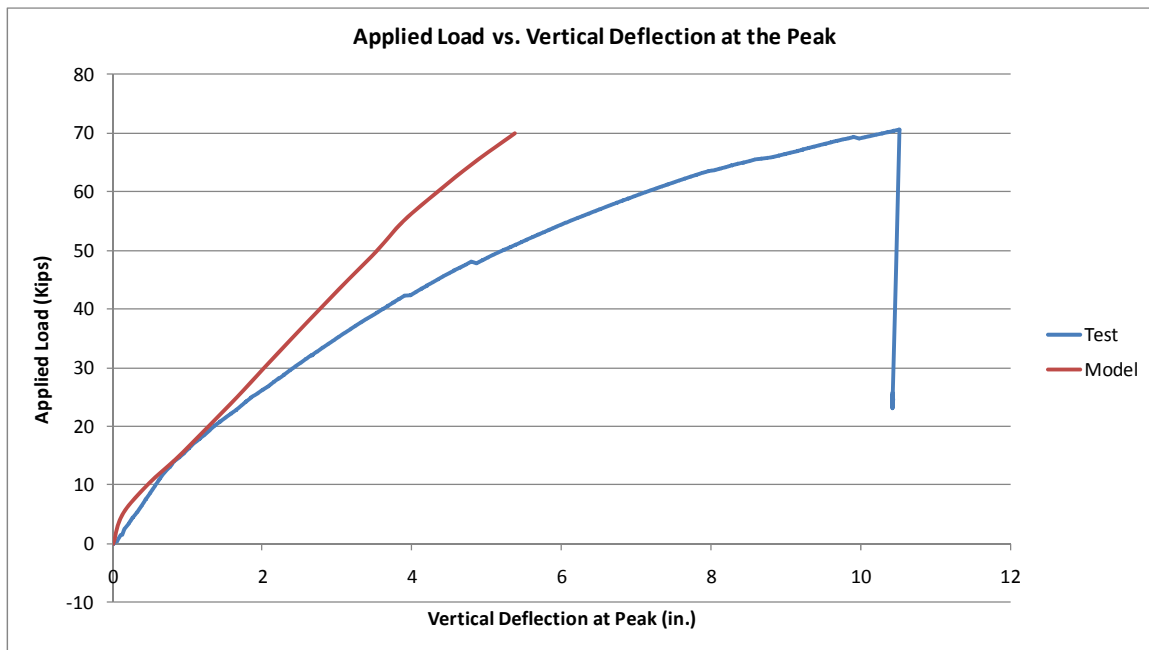


Figure 44. Vertical Load-Deflection Plot at Apex of Arch

Outputs from the model were not collected for the shoulders and base rotations though it is expected that the results would be similar to the behavior at the peak where there is reasonable agreement at the beginning of the test and less agreement as the arch got closer to failure. Figure 45 and Figure 46 show the horizontal and vertical deflections of the shoulders respectively. It can be seen that deflections of the arch were not completely symmetric. This can be seen more clearly in Figure 47 where the base rotation on the North side of the arch was roughly 38% greater than the rotation on the South side of the arch.

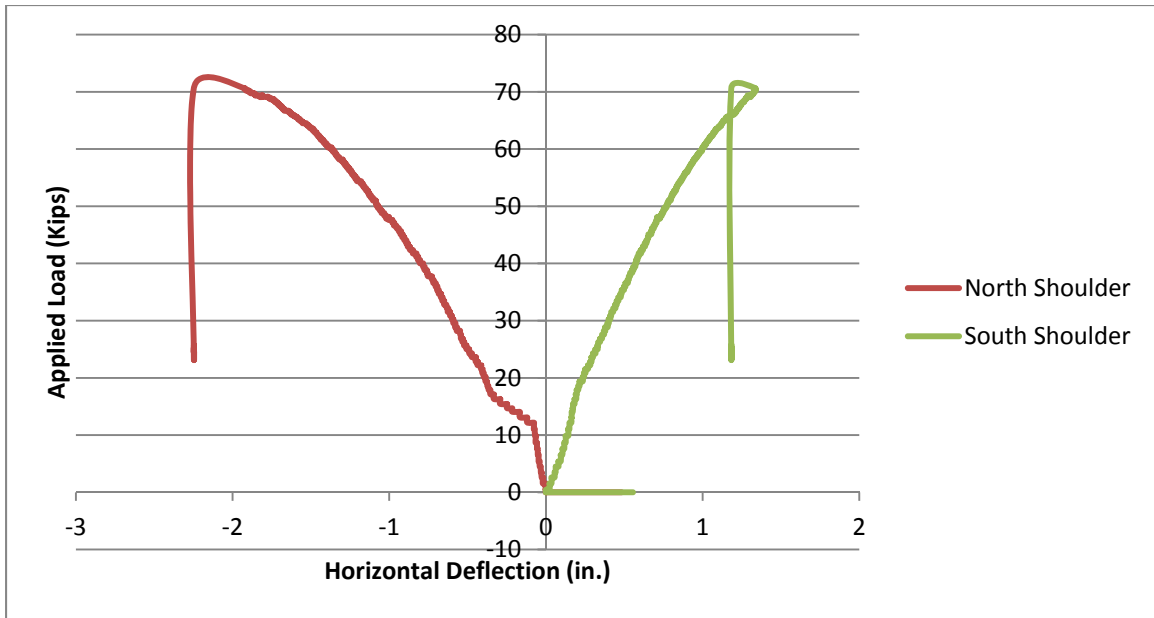


Figure 45. Load vs Horizontal Deflection At The Shoulders (Positive Is South)

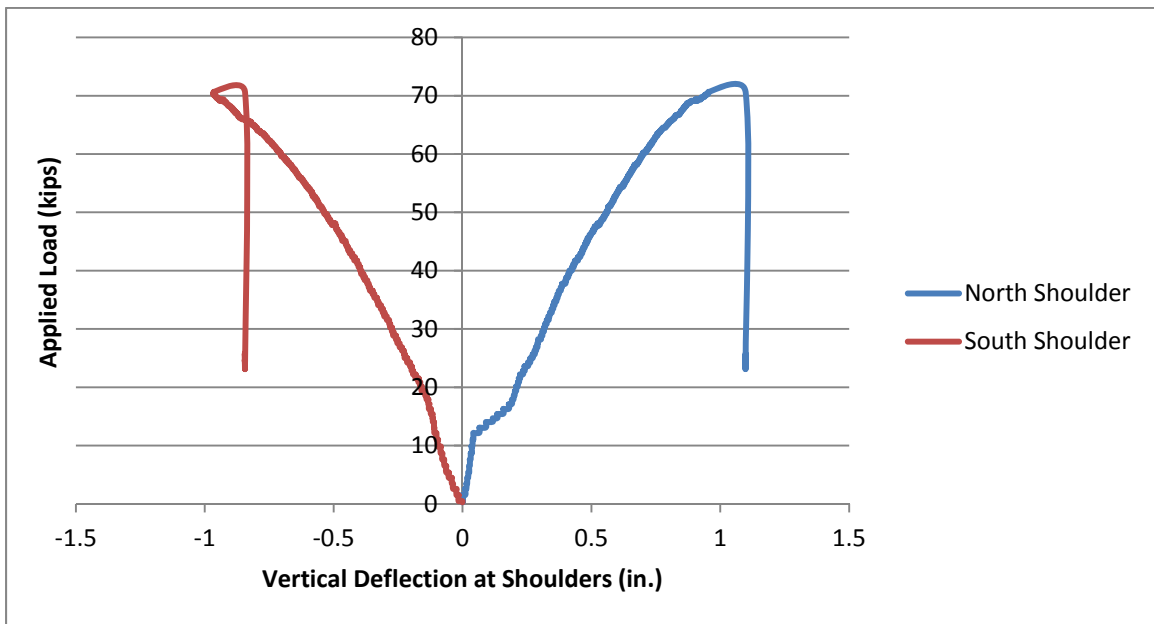


Figure 46. Load vs Vertical Deflection at the Shoulders (Positive Is Up)

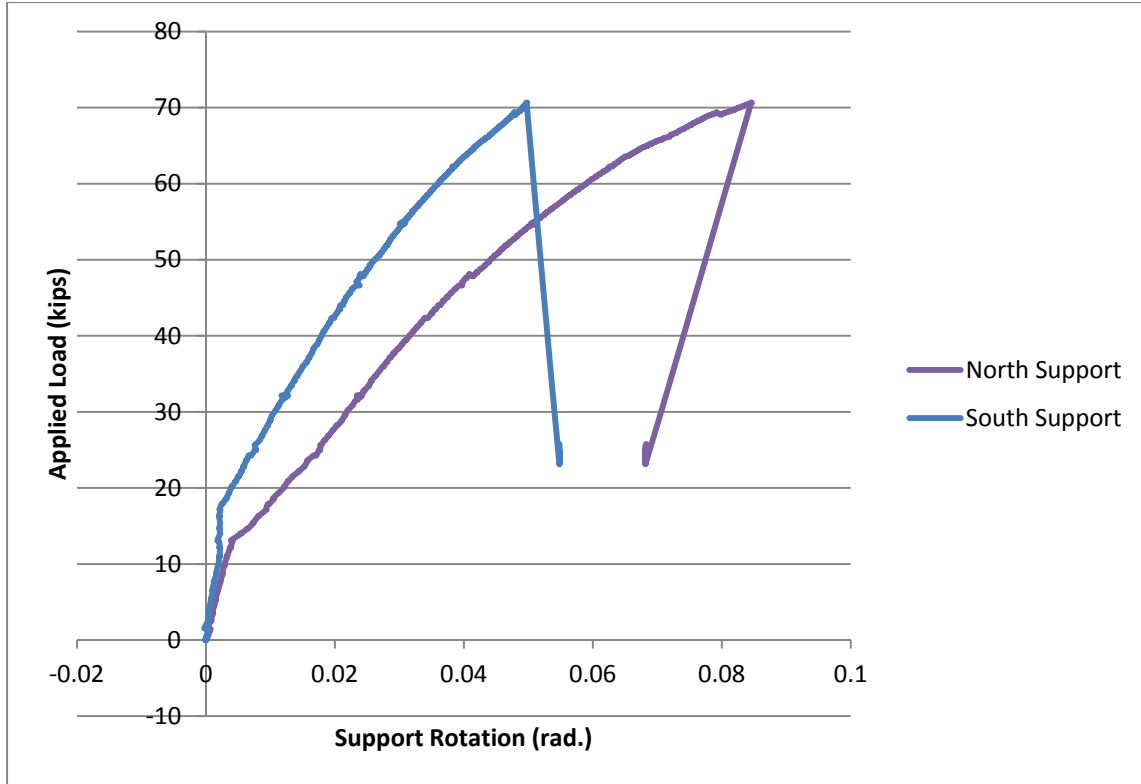


Figure 47. Applied Load vs Support Rotation

Conclusions

The arch testing results compared well with predicted capacities as well as failure modes. It did not however compare as well for deflections. This could be in part due to the uneven support rotations that took place during the test but was not modeled. Though the deflection at failure was not captured well, the beginning of the load-deflection plot is accurate up to roughly 33% of the failure load. This testing gives confidence to the modeling and design tools developed for designed the Bridge-in-a-Backpack™ bridges.

Fatigue Beam Testing

One 15 inch nominal diameter, 26 foot long CFRP beam was subjected to 2,025,758 cycles of fatigue and then statically tested to failure under 4-point bending. The fatigue range was taken as the service live load moment effects of the Perkins Bridge. The objective of this test was to evaluate the capacity of the beam subjected to fatigue loading corresponding to the equivalent of 75 years of service life per the commentary on page 6-42 of AASHTO (2007). Strength predictions versus testing results as well reductions in stiffness of the beam and plastic deformations were investigated.

Specimen

The beam was 15” nominal diameter with a length of 26 feet. The center-to-center spacing of the supports was 25 feet. This beam had the same fiber layup as the Perkins Bridge arches in Belfast, Maine. This fiber layup included one layer of glass and two layers of braided carbon fiber in a vinylester matrix. A portion of the test setup can be seen in the following figure.



Figure 48. Center Portion of Test Setup

Loading

The beam was loaded between the calculated service dead load moment and the calculated total service level moment in the Perkins Bridge according to design calculations. This resulted in an actuator load of 7.7 kip and 18.1 kip and moments of 416 kip-in and 975 kip-in for the dead load and total load service moments respectively. The predicted flexural capacity of the section is 2595 kip-inches and is controlled by compression failure. As a note the predicted failure flexural strength if tension controlled is 2812 kip-inches. The section is predicted to be compression controlled due to a lack of sufficient confinement. This lack of confinement is not as visible in the arch testing due to the loading frame on the compression face of the arch section.

Results

The failure moment from the final static test after over 2,000,000 cycles was 2783 kip-inches. It appears this beam may have failed in a combination of tensile rupture as all previous specimens have as well as in compression. The design tools and draft guide specification predict a compression failure with the level of glass confinement available in this specimen. The failure region at the midspan of the specimen can be seen in the following figure.



Figure 49. Failed Beam Specimen

The first approximately 150,000 cycles are not shown as there was an error during loading of the beam and it was overloaded to approximately 38 kips or 200% of the total service load moment. It was shown there after that overload there is minimal movement of the fatigue histogram with roughly an increase in deflection of 0.3 inches (15%) at the loading points of the beam. Cracking parallel to the length of the member could be seen near the mid-height of the section near midspan prior to failure. Additionally, at this crack the top half of the FRP shell ruptured and separated from of the member at failure over a distance of roughly two feet centered about midspan. Fiber rupture was seen on the tension face of the member, but not in the diamond pattern that is typically seen on these members. Compression capacity was a controlling factor in the ultimate capacity of this member.

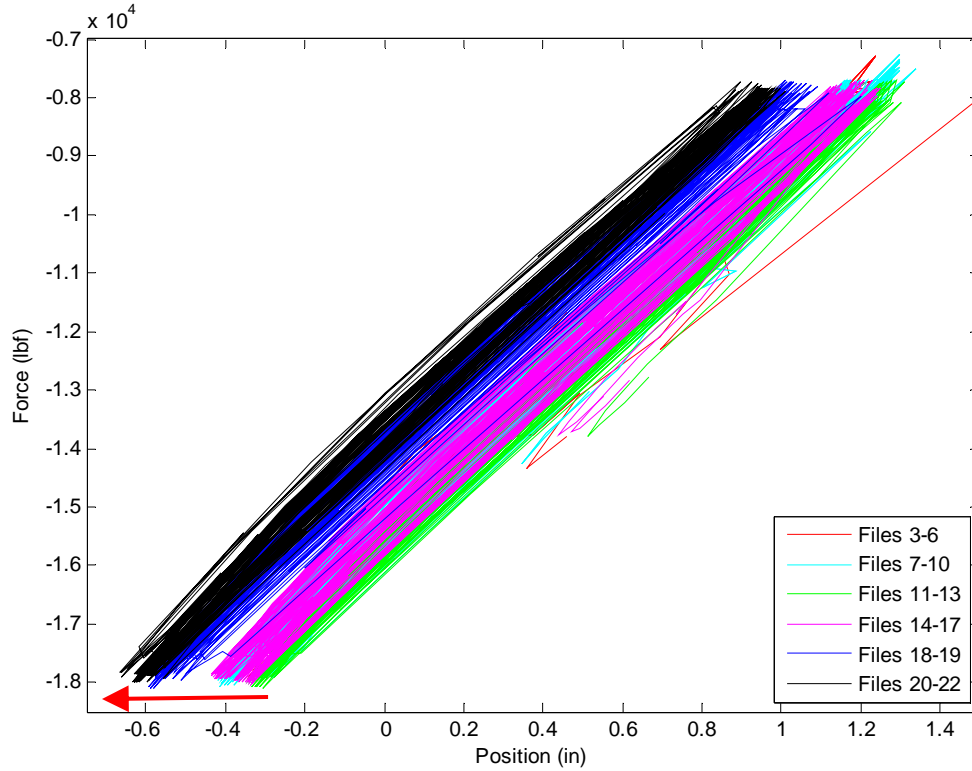


Figure 50. Load-Deflection Plot of Fatigue Beam Post Overloading

Moment versus strain can also be seen in Figure 51. As with the arch, moments in the beam at failure were similar to those predicted from design tools. The shapes of the plots appear consistent with previous testing and peak values are consistent with ultimate values known for the laminates and concrete. The ultimate longitudinal tensile strain of the laminate is 0.0157 per testing by Demkowicz (2011). As seen in Figure 51, the maximum strain recorded on the tension face of the specimen was roughly 0.015 in/in. This value is approximately 5% lower than the predicted value of 0.0157.

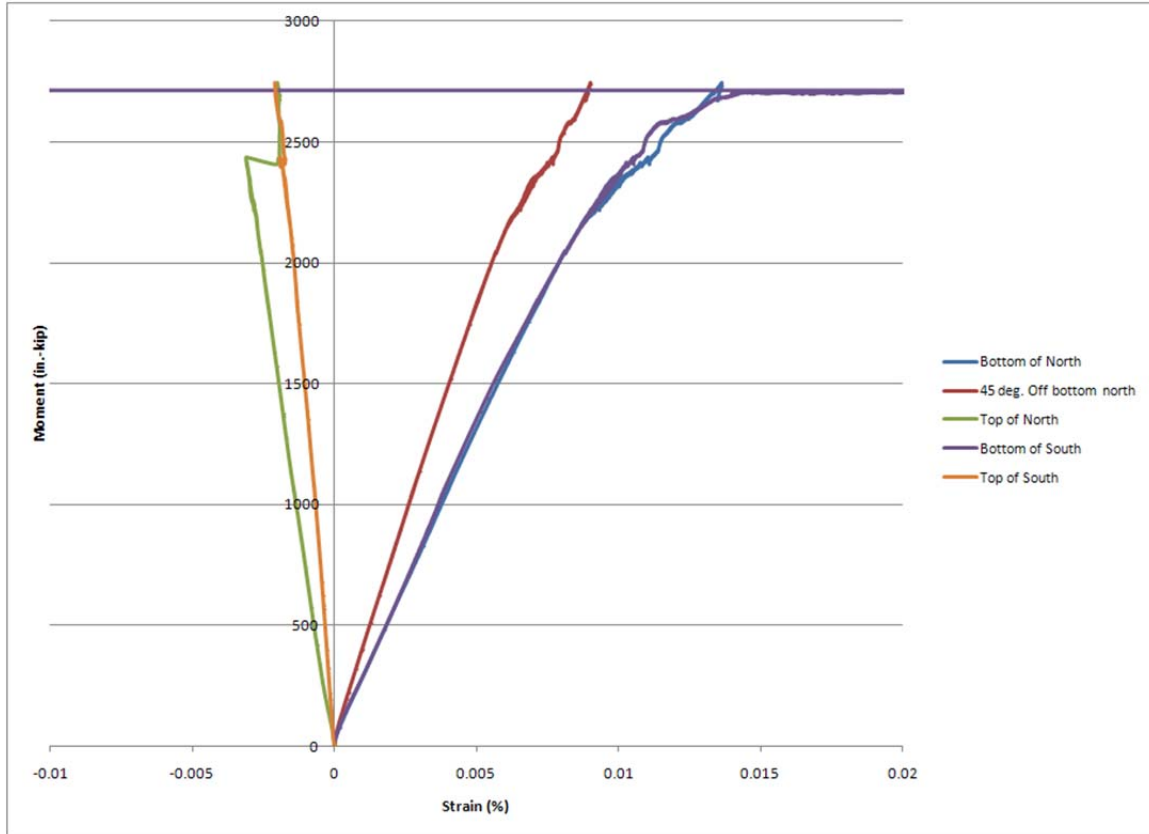


Figure 51. Moment vs Strain Plot of Beam to Failure

Conclusions

The fatigue beam testing demonstrated that the capacity for the larger diameter tubes after over 2 million cycles at the full service load level is equivalent to the predicted capacities for this representative case. It is expected that larger diameter tubes will not greatly affect the fatigue resistance of the beams and that conclusions from previous research holds true for the larger tubes (Bannon 2009).

Conclusions

Modeling, testing and manufacturing techniques were developed and refined to allow for longer span arches to be designed and manufactured for use in buried composite arch bridges. This work has included laboratory testing of a full scale arch as well as straight beams under static and fatigue loads. Models and specifications were in reasonably good agreement for the strength of the test specimens, though the deflection predictions were under-predicted for the arch. Predicted strengths for the tube were very close to the strength of the straight beams after 2,000,000 cycles of the full service live load predicted

for the Perkins Bridge in Belfast, Maine. Bracing schemes were designed to minimize shape change of the cross section during construction loads when there was no cured concrete in the tubes. Manufacturing refinements to allow for the use of larger diameter tubes included refined flow media and bagging materials, new end plug designs as well as new processes for handling these materials during fabrication. The filling process was also modeled and tested. A great deal of work went into developing analytical and numerical models to investigate the structural response of the hollow, tubular FRP arches to wet concrete loads. As a result, understanding of the response of the structure under construction loads is significantly improved, and uncertainty and design conservatism can be decreased during construction. This will give more efficient designs of the Bridge-in-a-Backpack™ structures in the future.

References

- AASHTO LRFD Bridge Design Specifications 4th Edition. American Association of State Highway Officials. Washington D.C. 2007.
- Bannon, Dan, Goslin, Keenan WI-T-77 “Static and Fatigue Testing of Cylindrical Concrete Filled FRP Beams”. AEWG Internal Work Instruction. AEWG Center June 26, 2008 rev Sept 2010.
- Bannon, Dan. “Characterization of Concrete-Filled Fiber Reinforced Polymer (FRP) Arch Members”. Master’s Thesis. University of Maine. May 2009.
- Clapp, Joshua, Davids, William. “CFRP Arch Analysis and Theory”. AEWG Technical Report 11-30. University of Maine. January 31, 2011.
- Demkowicz, Mackenzie. “Environmental Durability of Hybrid Polymer Matrix Composites for Infrastructure Application”. Master’s Thesis. University of Maine. May 2011.
- Fam, Amir, et al. “Proposed AASHTO LRFD Guide Specifications for Design of Concrete-Filled FRP Tubes for Flexural and Axial Members.” AASHTO. Washington D.C. December 20, 2010.
- “Technical Data and Design Guide. Fiberglass-Reinforced Plastic Roofing/Siding Panels Roof Deck, Gutter Systems, Louvers & Ridge Vents”. Enduro Composites. Houston, TX. 2002
- Mostoller, Jeremy. “Arch Sheathing Panel: Global sizing Verification”. Engineering report from Creative Pultrusions, Inc. to Advanced Infrastructure Technologies, LLC. January 20, 2011.
- Walton, Harold. “Response of FRP Arches to Concrete Filling Loads”. Master’s Thesis. University of Maine. May 2011.
- Faraji S, Ting JM, Crovo DS, Ernst H (2001). Nonlinear analysis of integral bridges: finite-element model. *Journal of Geotechnical and Geoenvironmental Engineering*, 127(5): 454-461.
- NCHRP (1991). *Manuals for the Design of Bridge Foundations*. National Cooperative Highway Research Program Report No. 343, Transportation Research Board, Washington, DC.
- Ting JM and Faraji S (1998). *Force-Displacement Testing for Integral Abutment Bridges*. University of Massachusetts Transportation Center Report No. UMTC 97-13, University of Massachusetts, Amherst, MA.

USACoE (1994). *Design of Sheet Pile Walls*. CECW-ED Engineer Manual 1110-2-2504.
Department of the Army, US Army Corps of Engineering, Washington, DC.